Monte Carlo Simulations of Phase Distribution in Porous Materials

by

Benjamin D. Zeidman

A thesis submitted to the Faculty and the Board of Trustees of the Colorado School of Mines in partial fulfillment of the requirements for the degree of Doctor of Philosophy (Applied Chemistry).

Golden, Colorado

Date _____

Signed: _____
Benjamin D. Zeidman

Signed: _____
Dr. David Wu
Research Advisor &
Professor and Department Head of Chemistry

Signed: _____
Dr. Ning Lu
Co-Research Advisor &
Professor of Civil and Environmental Engineering

ABSTRACT

The interplay and absorption of gases and fluids within a pore space is a fundamental phenomenon of natural systems. In particular, the equilibrium phase distribution of these components within the porous material affect many of the constitutive properties of these materials. These effects can be far ranging from stability of hill slopes resulting from partially saturated soil to the recovery of gas and oil within sediments for energy applications. Therefore a critical understanding and investigation of the equilibrium phase distribution within porous materials is desired.

To address this, we have developed a robust Monte Carlo simulation methodology. The methodology uses a lattice gas with nearest neighbor interactions to model the equilibrium phase distribution of the constitutive materials. A primary goal in developing this methodology was to allow direct input of experimental pore space information and to allow prediction of properties for specific porous systems. Input variables such as the pore geometry and interfacial free energy values are thus all calculated directly from experimental values. Systems of water, air, and solid at both constant volume (canonical) and constant humidity (grand canonical) simulation conditions gave results that were in excellent agreement with experiment. Specifically, quantitative agreement was achieved for the soil-water retention curve in both canonical and grand canonical systems and equilibrium phase distribution between simulation and experimental imaging. The methodology was also applied to systems of gas hydrate and oil recovery from within sediments.

TABLE OF CONTENTS

LIST OF FIGURES

ACKNOWLEDGEMENTS

It goes without saying that no undertaking is possible without the love and support of friends and family. Thank you to everyone who has been a part of my life on this journey. While only one author is listed on the front of this work, you all share an equal contribution to its contents.

Thank you to my advisors, Dr. David Wu and Dr. Ning Lu, your mentorship has been invaluable over these long years. Thank you to my research group for your friendships and all the time you spent both listening to and helping me.

Thank you to my collaborators, Dr. Clinton Willson for the experimental imaging data and Dr. Alexandra Wayllace for the Ottawa TRIM studies.

Finally, thank you to the financial support from the Department of Chemistry and Geochemistry and Dr. Azra Tutuncu and the CSM Unconventional Natural Gas and Oil Institute.

CHAPTER 1
INTRODUCTION

The adsorption and interplay of liquids and gases when confined within a porous material is a fundamental process occurring in nature. As such, study of the interactions between the various phases within a solid pore space is of considerable interest and has many avenues of active research. The scope of this dissertation investigates the equilibrium distribution of various phases when confined within a pore space by means of a coarse-grained Monte Carlo lattice simulation methodology. The chapters within this dissertation are organized as a series of journal articles published by various scientific entities.

1.1. Dissertation Organizational Structure and Outline

Chapter 2 serves as a review of various literature topics not covered in the subsequent chapters. These topics include an introduction to capillarity, experimental methods for measuring water retention in porous media, and other simulation methodologies. These additional simulation techniques address phase equilibria within a pore space in addition to fluid transport and hysteresis.

Chapter 3 is a book chapter published by World Scientific in the book *Pore Scale Phenomena: Frontiers in Energy and Environment*. This Chapter serves as a general overview of the work detailed in this dissertation and includes a description of the coarse-grained Monte Carlo methodology, relation to current literature, and some results obtained for canonical (constant volume) and grand canonical (constant chemical potential) simulation of fluids within a mesoporous material. The pore space

geometry is representative of Ottawa sand and obtained directly from experimental imaging techniques.

Chapter 4 is a journal article published by *Geophysical Research Letters* and further explores the concept of canonical, or constant volume, simulation. The methodology is detailed and applied to various systems. All of the systems included are modeled for water adsorption within pore spaces of increasing geometric complexity. The simplest case looks at water adsorption between two spheres in contact. Increasing in geometric complexity is the investigation of a pore space based on randomly distributed spheres. Specifically, the pore space geometry was taken directly from experimental images of equilibrium water distribution within a series of randomly distributed glass spheres. The final system examined is a pore space geometry again taken directly from experimental imaging of a sample of Ottawa sand. In the cases of randomly distributed spheres and Ottawa sand, simulation shows excellent agreement with experiment for both capillary phase distribution and constitutive properties such as soil-water retention and capillary specific surface area.

Chapter 5 is an article submitted to the Journal of Chemical Physics. This chapter is an in-depth examination of the hysteresis seen when a pore space undergoes wetting or drying. This is accomplished through the use of a grand canonical coarse-grained Monte Carlo simulation. As opposed to canonical simulation where the volume of water is specified, grand canonical simulation instead specifies a chemical potential and allows the volume of water within the simulation to vary. The simulation domain is initially completely dry for the case of wetting, or fully saturated for the case of drying. Under constant chemical potential the saturation level of water is allowed to

equilibrate. Two pore space geometries are considered: randomly distributed spheres and Ottawa sand as used in the previous chapters. Various properties are calculated include isothermal adsorption curve, soil water-retention, and an examination of simulation equilibrium. Results show good correlation with experiment.

Chapter 6 investigates the adsorption phenomena of multiple fluids confined within a pore space. Two systems are investigated. The first is a system with a wetting fluid and a non-wetting fluid analogous to water and clathrate hydrates. I investigate the hydrate distribution within sediment assuming a hydrate formation in solution assuming equilibrium on geologic timescales. The second system examines the case of two wetting fluids competitively wetting the same pore space. This is representative of a system of water and oil. The contact angle is manipulated to investigate how the two fluids are distributed within the pore space. The pore space geometry considered includes simple system of two square-shaped pores of different sizes, a system of randomly distributed ink-bottle and slit pores, and Ottawa sand.

Chapter 7 summarizes the results of the previous chapters and discusses their significance and relation to the project overall. A discussion of future work is included.

Three appendices are included describing simulation methodology, experimental methodology, and copyright, reprinting, and coauthor permissions.

1.2. Approach and Goals

The connection of macroscopic properties to the distribution and complex interplay of fluids and gases within pore space is not fully understood. The scope of this work is to develop a coarse-grained Monte Carlo simulation methodology that is designed to mimic as closely as possible specific experimental systems. To facilitate

this goal, the simulation was designed so that all variables input into the methodology are obtained from experimental studies. Two simulation variables dominate the methodology: pore space geometry and phase interaction. Pore space geometry is represented in two dimensions as cross-sectional slices of the full three-dimensional pore space taken directly from experimental imaging, and then discretized into a simulation lattice. While the methodology is fully general in being applicable to three dimensions, this two-dimensional representation allows numerical efficiencies relative to three-dimensional simulation, with quantitative determination of three dimensional properties by standard stereological methods. Phase interaction variables, otherwise known as the coupling parameters, are obtained either from literature values for surface tension or experimental measurements of the contact angle.

The result is a robust simulation methodology capable of determining equilibrium capillary distribution of multiple phases of liquids and gases confined within a pore space. Pore spaces can range in size from the nanoscale to the mesoscale. Simulation can include any amount or type of wetting and non-wetting phases provided basic experimental properties of interaction (surface tension or contact angle) are known. This yields an important tool for the investigation of adsorption phenomena within porous materials.

CHAPTER 2
LITERATURE REVIEW

This chapter presents a review of relevant literature on topics not covered in the other chapters. This section is not exhaustive as Chapter 3 serves as a more relevant literature review and sets the context of how the work contained herein fits within the broader context of pore scale science.

2.1. Studies of Capillarity and Pore Geometry

Several approaches have been taken to explore capillarity and pore geometry in porous media. These range from simulation methodologies to experimental imaging techniques exploring both capillarity and transport within a pore network.

Randive et al (2014) [1] investigated capillarity-wettability interactions in non-wetting phases using a lattice Boltzmann methodology. Surface wettability and geometry in a two phase system within a pore channel were analyzed. The study suggested that the effects of capillarity can be altered by exciting the nonwetting phases with acoustical resonance. The transporting of non-wetting phases can be measured with frequencies close to a resonant frequency and in mobilizing species trapped to the non-wetting phases, with applications in areas such as oil and two phase flows.

Han et al (2009) [2], studied the connectedness of a capillary pore network using the electrical conductivity in partially saturated porous media. The study showed that Archie's law [3] is followed at high saturation levels. However, for saturations below approximately 20% volume fraction water, a deviation from Archie's law was seen. The authors hypothesized that creating a wetting layer with brine solution can result in the

system following Archie's law even at low saturations. Using a Monte Carlo lattice gas methodology, two protocols were tested to distribute the brine in the pore network imaged with three dimensional micro-tomography. A random walk method was used to calculate the electric conductivity. The first method was a simulated annealing minimization of interfacial energy while the second took into account the quasistatic capillary displacement. The simulated annealing method showed a more realistic menisci distribution of the brine solution at saturations below ~40% volume fraction water.

Udell (1985) [4] presented a study of the heat and mass transfer though a porous media from a theoretical approach with direct comparison to experimental data. The theoretical model was based on a one dimensional steady state system consisting of a single component fluid filled porous media. The system had a heated end and a cooled end resulting in three distinct regions: a vapor zone adjacent to the heating side, a two phase zone, and a liquid zone next to the cooled side. The effects of capillarity, gravity forces and phase changes were included. The experimental system consisted of a fiberglass channel filled with Ottawa sand with several grain sizes. The sand core was heated from the top and the bottom was held at a constant cold temperature. The use of ten identically spaced thermocouples were used to record the temperature. The theoretical and experimental results had good correlation. The major results are summarized as capillarity of the single component fluid acted against the flow of the two phases in the two phase region, the liquid saturation profile is independent of heat flux, the temperature flux across the two phase zone increases with decreasing permeability,

and the effective thermal conductivity of the two phase zone is several orders of magnitude greater than the conductivity in the single phase zones.

Blokhuis and Kuipers (2007) [5] investigated the structure and tension between a fluid and spherically shaped hard wall. Their primary goal was to investigate expressions for the Tolman length [6] (deviation of surface tension from its planer value) using a density functional approach with van der Waals squared-gradient theory. Although this approach does not obey thermodynamic relations for a liquid interface at a solid wall, mechanical equilibrium is preserved. For a fluid in contact with a hard wall, the wall theorem and contact theorem state that the density at the wall is linked to pressure. The condition of mechanical equilibrium between the solid wall and the fluid phase was verified for a coexisting liquid and fluid or vapor phase. The study linked the Tolman length to classically determined interface properties derived from the density, vapor pressure, and temperature.

2.2. Hydrates in Sediments

This section examines several literature studies that look at the modeling of gas or methane hydrate formation and dissociation within sediments and porous materials. The applications include hydrate-methane-water phase diagrams, mathematical models of hydrate formation, and applications of experimental methodology to hydrate formation.

Gering et al (2006) [7] presented equations for the methane-water-hydrate phase diagram including temperature and pressure as a function of partial molar volume of dissolved methane. The production of dissolved methane could be a result of biogenesis or thermogenesis. The gas can be trapped in sediments and hydrate

stability conditions can be assessed. Reflectors are seen in seismic images of hydrate forming areas and caused by seismic contrast in a free gas zone, trapped in a layer of hydrate. Homogeneous sediments have no apparent lithologic traps and the hydrate layer provides a trapping mechanism, although the permeability of such layers is questionable or uncertain. Metastability of hydrate formation requires free gas and substantial sub-cooling and results in formation of hydrate crystals. The types of methane sources are either local sources in hydrate and free gas zones or remote sources with methane transported through homogeneous sediments and faults in the sediment. The temperature of the hydrate stability zone is considered to be too low for thermogenesis of methane and so the sources of methane are considered to be methanogenic microorganisms. The temperatures for these organisms to produce methane are low and pressures high compared to hospitable conditions for most organisms, and so such organisms exist in ocean sediments. The organisms are active as the methane tends to accumulate until the formation of gas bubbles as free gas accumulates and are held in sediments. The sediments are an alternative source of methane with temperatures high enough for thermogenesis, although at shallow points temperatures are typical where microorganisms are active. The methane is transported into sediment columns as bubbles or dissolved in water. Bubbles rise through water until getting trapped on the sea floor. Soluble methane in homogeneous sediment shows how free gas might be formed and trapped and hydrate formation usually is unable to explain free gas formation [7].

Mohammadi et al (2012) [8] modeled gas hydrate phase equilibrium in porous media. First they determined a correlation between hydrate suppression temperature as

a result of the pore confinement effects on the ice point depression. They then developed a regression model to predict when hydrate dissociation occurs. The porous media studied include silica gel, porous silica glass, mesoporous silica meant to mimic sediments. Showing a linear relationship between ice point depression in porous media and hydrate dissociation temperature, they were able to show good agreement with hydrate dissociation data from the literature. This suggests that this application can reduce the need to tune thermodynamic models for hydrate formation in porous media.

Stern et al (2011) [9] investigated core sections recovered from the Mount Elbert Gas Hydrate Stratigraphic Test Well on the Alaskan North Slope. Experimental imaging techniques of cryogenic scanning electron microscopy and powder X-ray diffraction to investigate the sediment and pore structure as well as the adsorbed hydrate phase within the pore space. Cryogenic SEM showed that gas hydrate phases occur primarily in a pore-filing geometry and sediment grains have approximately 75% saturation. Pore throat diameters show a common range of 20–120 microns. X-ray analysis and imaging of the sediment phase showed predominantly fine-grained sand and feldspar as well as muscovite and minor clays. Gas chromatography was employed to determine that the composition of the hydrate phase was mostly methane with trace amounts of carbon dioxide and ethane. Texture and composition of hydrate laden sediments can have significant impact on measurable properties of the material such as thermal, electrical, and acoustic conductivity. These can be correlated with the mechanical strength of the sediment.

Anderson et al (2003) [10] presented an experimental investigation of equilibrium and melting of various hydrate systems in mesoporous silica glass. Equilibrium data for

methane, carbon dioxide, and methane-carbon dioxide hydrates were obtained. The experiments were performed in a high pressure cell with supersaturated solutions of distilled water and gas. High capillary pressures could result in depressed solid decomposition temperatures including dissociation and ice melting and clathrate dissociation. The data are important for thermodynamic modeling in hydrates and this could also be important in sedimentary environments that are useful in the simulation of potential methane hydrate exploitation and carbon dioxide sequestration. They demonstrated that small diameter pores have a capillary inhibition effect on the equilibrium dissociation conditions for clathrate hydrate. Thus, pore size has a major effect on the stability of hydrate in sediments.

Clarke and Bishnoi (2005) [11] demonstrated the usefulness of FBRM to monitor particle size evolution and measure hydrate formation rates. Hydrate formation in hydrocarbon liquids has been difficult to measure and model. The formation of large amounts of hydrate can be modeled by separate considerations of mass transfer, heat transfer and intrinsic kinetics. The development of hydrate particles is used to examine hydrate particle growth mechanisms as found in water in crude oil dispersions. Water droplets were monitored alongside hydrate particle size distributions.

These findings that pore space size and geometry can affect hydrate formation, equilibration, and dissociation echo results found in experimental studies such as those of Vysniauskus and Bishnoi (1983), showing the effect of interfacial area on hydrate formation [12], and the detailed experiments on hydrate formation and particle size distribution of Englezos et al (1987) [13].

2.3. Capillarity Modeling Techniques

This section describes several studies used to model capillarity in pore systems. The techniques used include simulated annealing, lattice Boltzmann, and numerical fluid dynamics methods. Pore systems include both mesoscale and nanoscale and are derived from simple geometric models to systems reconstructed from experimental imaging data.

Galani et al (2007) [14] described several simulation techniques and investigated transport phenomena in porous structures with three fluid phases: wetting phase, intermediate wetting phase, and non-wetting phase. The spatial distribution of fluid phases inside the pore structures is determined through minimization of interfacial energy and a simulated annealing scheme was used to find the optimal configuration that renders it efficient across all saturation levels. The distribution of fluid phases found in single and multipore domains shows the combination of digital reconstruction using annealing techniques that model multiphase systems.

The methods are based on prediction of absorption and transportation properties in porous materials that are used to explain behavior of the two fluid phases. Tracer diffusion was characterized in a random sphere packing with three fluid phases. There is also a flow of one fluid phase through the same porous structure as the pore space is occupied by two immobile fluid phases. The diffusivities are calculated with a random walk method and relative permeabilities are measured employing a Stokes equation using a finite-difference scheme and an artificial compressibility relaxation algorithm. The transport properties of wetting and non-wetting phases are in agreement with data and this is independent of whether the pore space is occupied by two or three fluid

phases. The transport properties reinforce the reliability of proposed fluid phase distribution techniques as well as effective diffusivities and relative permeabilities [14].

The spatial distribution of the three fluid phases inside porous structures is important in a wide range of technological activities including oil recovery, food engineering, and hazardous waste distribution and disposition. Spatial distribution of phases strongly affects the properties of composite media and their thermal and electrical conductivities. Some of the other properties that are affected are trace diffusivity, dielectric constant, compressional wave velocities, and relative permeability. The prediction of the configuration of fluid phases in porous domains could be nontrivial primarily due to complex pore space morphologies and the dynamic interaction between distribution of fluid phases and processes due to pore confinement. Computer aided studies of composite media have been enhanced by digital reconstruction methods where binary domains represent pore space topology at the mesoscopic level. Techniques using information from digital reconstruction could help determine parameters that favor properties that are more desirable [14].

If more than one fluid phase is present in the pore space, it is necessary to obtain a reliable distribution of phases within the reconstructed domains before proceeding with predictions of macroscopic properties. An attractive mesoscopic method based on simulated annealing is proposed to determine the distribution of liquid phases in binary domains. For intense momentum transfer processes, a reliable approximation for systems would be needed for thermodynamic equilibrium. Such equilibrium configurations could aid in the distribution of vapor and condensate during adsorption within porous media. The macroscale distribution of fluid phases in geologic materials is

affected by gravity although each phase in not macroscopically uniform in a porous medium. At the meso and micro scales, interfacial forces dominate and so gravity is neglected. The simulated annealing technique for prediction of air-water interfacial area in porous media could be used for calculating thermal conductivity from two dimensional cuts of geologic media [14].

Berkowitz and Hansen (2001) [15] obtained the water distribution in partially saturated sandstone microstructures and examined the dependency of small sample electrical conductivity on saturation. The capillary condensation in mesoporous media was studied and the relative permeability of two fluid phase distributions was obtained with a simulated annealing approach. These techniques used in porous systems containing more than two fluid phases could aid in fluid recovery processes, for instance in water air containing soil. It is thus desirable to develop a fast technique for predicting the distribution of multiple fluid phases in a porous medium.

Hazlett and Vaidya (2002) [16] discussed the lattice Boltzmann method for simulating multiphase fluid dynamics and calculating preferential fluid interactions with solid walls. The contact angles were calibrated and wall interaction parameters showed pressure differences across interfaces. In simulation using the lattice Boltzmann method, fluid drops were forced down straight tubes and dynamic contact angles were observed. The simulations aided in the observation of dynamic contact angles in convergent and divergent systems. Hysteresis effects showed the phenomenon of contact angle was not a result of hydrodynamic interactions with equilibrium wetting conditions. The authors stated that the lattice Boltzmann models and similar forms of

simulation must incorporate the dynamic rock–fluid interactions that may be different from static interactions to explain the process of preferential wetting.

Joekar-Niasar and Hassanizadeh (2011) [17] developed a dynamic pore network model for simulation of a two phase flow in porous media and applied the model to non-equilibrium drainage and imbibition processes. They modeled the pore space with a regular three dimensional lattice consisting of truncated octahedron and parallelepiped interconnected pore structures. The primary driving force is the capillary pressure of the two respective phases. The two phase flow formulations show that the pressure difference between the two phases equals the capillary pressure, which is assumed to be a function of saturation, and is referred to as a non-equilibrium capillarity effect. The non-equilibrium capillarity theory is formulated as a function of saturation viscosity ratio and effective viscosity.

Magnani et al (2000) [18] presented a methodology for determining the interface of wetting and non-wetting phases in a three dimensional pore space at equilibrium. The pore space geometry is developed from two dimensional cross sections of experimental systems (e.g. Berea sandstone) and a random walk method is used to extrapolate a hypothetical three dimensional pore network. The authors use the Laplace-Young equation to numerically saturate the pore network at a given equilibrium state.

Tan and Piri (2015) [19] investigate fluid phase equilibria in nanopores using a perturbed-chain statistical associating fluid theory couple with the Laplace equation. The pore filling is modeled using the mechanical equilibrium between the vapor phase and the adsorbed liquid phase. Saturation levels are set by using equilibration to add subsequent thin films to the pore walls. The mechanical equilibrium is driven by the

capillary pressure. The pore size is used to calculate the Tolman length and applied to the value of the surface tension. The perturbed-chain statistical associating fluid theory calculates the Helmholtz energy arising from the various molecular interactions in the fluid phase and with the pore space. Simulations were performed in a pore space geometry based on cylindrical pores of various nano-scale sizes and Vycor glass. The study showed a correlation between the pore size and the pore critical temperature. This model was not validated with any experimental data.

2.4. References Cited

[1] P. Randive, A. Dalal, and P. P. Mukherjee, “Lattice Boltzmann modeling of two-phase behavior under acoustic excitation: Capillarity–wettability interaction,” *Int. J. Heat Mass Transf.*, vol. 74, pp. 460–472, Jul. 2014.

[2] M. Han, S. Youssef, E. Rosenberg, M. Fleury, and P. Levitz, “Deviation from Archie’s law in partially saturated porous media: Wetting film versus disconnectedness of the conducting phase,” *Phys. Rev. E*, vol. 79, no. 3, p. 031127, Mar. 2009.

[3] G. E. Archie, “The Electrical Resistivity Log as an Aid in Determining Some Reservoir Characteristics,” *Trans. AIME*, vol. 146, no. 01, pp. 54–62, Apr. 1942.

[4] K. S. Udell, “Heat transfer in porous media considering phase change and capillarity—the heat pipe effect,” *Int. J. Heat Mass Transf.*, vol. 28, no. 2, pp. 485–495, Feb. 1985.

[5] E. M. Blokhuis and J. Kuipers, “On the determination of the structure and tension of the interface between a fluid and a curved hard wall.,” *J. Chem. Phys.*, vol. 126, no. 5, p. 054702, Feb. 2007.

[6] R. C. Tolman, “The Effect of Droplet Size on Surface Tension,” *J. Chem. Phys.*, vol. 17, no. 3, p. 333, Dec. 1949.

[7] K. L. Gering, R. S. Cherry, and D. M. Weinberg, “Mechanisms for Methane Gas Accumulation under Hydrate Deposits in Sediments,” *Ann. N. Y. Acad. Sci.*, vol. 912, no. 1, pp. 623–632, Jan. 2006.

[8] A. H. Mohammadi, A. Eslamimanesh, D. Richon, F. Gharagheizi, M. Yazdizadeh, J. Javanmardi, H. Hashemi, M. Zarifi, and S. Babaee, “Gas Hydrate Phase Equilibrium in Porous Media: Mathematical Modeling and Correlation,” *Ind. Eng.*

Chem. Res., vol. 51, no. 2, pp. 1062–1072, Jan. 2012.

[9] L. A. Stern, T. D. Lorenson, and J. C. Pinkston, “Gas hydrate characterization and grain-scale imaging of recovered cores from the Mount Elbert Gas Hydrate Stratigraphic Test Well, Alaska North Slope,” *Mar. Pet. Geol.*, vol. 28, no. 2, pp. 394–403, Feb. 2011.

[10] R. Anderson, M. Llamedo, B. Tohidi, and R. W. Burgass, “Experimental Measurement of Methane and Carbon Dioxide Clathrate Hydrate Equilibria in Mesoporous Silica,” *J. Phys. Chem. B*, vol. 107, no. 15, pp. 3507–3514, Apr. 2003.

[11] M. A. Clarke and P. R. Bishnoi, “Determination of the intrinsic kinetics of CO gas hydrate formation using in situ particle size analysis,” *Chem. Eng. Sci.*, vol. 60, no. 3, pp. 695–709, Feb. 2005.

[12] A. Vysniauskas and P. R. Bishnoi, “A kinetic study of methane hydrate formation,” *Chem. Eng. Sci.*, vol. 38, no. 7, pp. 1061–1072, 1983.

[13] P. Englezos, N. Kalogerakis, P. D. Dholabhai, and P. R. Bishnoi, “Kinetics of gas hydrate formation from mixtures of methane and ethane,” *Chem. Eng. Sci.*, vol. 42, no. 11, pp. 2659–2666, 1987.

[14] A. N. Galani, M. E. Kainourgiakis, N. I. Papadimitriou, A. T. Papaioannou, and a. K. Stubos, “Investigation of transport phenomena in porous structures containing three fluid phases,” *Colloids Surfaces A Physicochem. Eng. Asp.*, vol. 300, no. 1–2, pp. 169–179, Jun. 2007.

[15] B. Berkowitz and D. P. Hansen, “A Numerical Study of the Distribution of Water in Partially Saturated Porous Rock,” pp. 303–319, 2001.

[16] R. D. Hazlett and R. N. Vaidya, “Lattice Boltzmann simulations and contact angle hysteresis in convergent–divergent media,” *J. Pet. Sci. Eng.*, vol. 33, no. 1–3, pp. 161–171, Apr. 2002.

[17] V. Joekar-Niasar and S. Majid Hassanizadeh, “Effect of fluids properties on non-equilibrium capillarity effects: Dynamic pore-network modeling,” *Int. J. Multiph. Flow*, vol. 37, no. 2, pp. 198–214, Mar. 2011.

[18] F. S. Magnani, P. C. Philippi, Z. R. Liang, and C. P. Fernandes, “Modelling two-phase equilibrium in three-dimensional porous microstructures,” *Int. J. Multiph. Flow*, vol. 26, no. 1, pp. 99–123, Jan. 2000.

[19] S. P. Tan and M. Piri, “Equation-of-state modeling of confined-fluid phase equilibria in nanopores,” *Fluid Phase Equilib.*, vol. 393, pp. 48–63, May 2015.

CHAPTER 3

COARSE-GRAINED MONTE CARLO SIMULATION OF THE DISTRIBUTION AND CAPILLARITY OF MULTIPLE FLUIDS IN POROUS MEDIA

A paper published in Pore Scale Phenomena: Frontiers in Energy and Environment[1]

Benjamin D Zeidman[2,3], Ning Lu[4], and David Wu[5]

3.1. Abstract

The pore-scale distribution of fluids and gasses and the associated capillary phenomena control key macroscale constitutive properties of interest in any porous medium, including systems of water or oil in soils and rocks. However, due to the geometric complexity of the pore space as well as that of interfaces between phases, the distribution of fluids and forces is difficult to obtain. An attractive approach for efficient determination of the spatial distribution of various fluid components--such as air, water, oil, or gas hydrate--in a porous medium is Coarse-Grained Monte Carlo simulation. The method is well-suited to handle complicated pore space geometries, and can exploit advances in imaging technologies such as X-ray micro CT for obtaining high-resolution maps of pore space. Coarse-graining allows for computational

---

[1] Reprinted with Permission of World Scientific: B.D. Zeidman, N. Lu, and D. Wu, "Coarse-Grained Monte Carlo Simulation of the Distribution and Capillarity of Multiple Fluids in Porous Media" in Pore Scale Phenomena: Frontiers in Energy and Environment, edited by J. Poate, T. Illangasekare, H. Kazemi, and R. Kee (World Scientific, Singapore, 2015), pp. 263-278.

[2] Graduate Student, Department of Chemistry and Geochemistry, Colorado School of Mines.

[3] Primary researcher and author.

[4] Department of Civil and Environmental Engineering, Colorado School of Mines.

[5] Department of Chemistry and Geochemistry, Colorado School of Mines.

efficiency, and can be applied at the inherent size scale of the pores, from nano to macro scale. Monte Carlo simulation foregoes expensive, explicit simulation of hydrodynamic transport, to allow rapid determination of local equilibrium phase distributions.

While Coarse-Grained Monte Carlo has been used before to simulate adsorption in porous media, we make parallel measurements on an experimental system (Ottawa sand) and simulations based on the experimentally determined pore space of the same system, and demonstrate excellent agreement in key constitutive properties including capillary pressure, soil-water retention, specific surface areas, as well as wetting/drying hysteresis. To do this, we introduce a method for using two-dimensional slices of the 3D pore space for efficiency. Our results support the hypothesis that Coarse-Grained Monte Carlo generates metastable configurations consistent with experimental hysteresis, justifying our elimination of Simulated Annealing used in prior approaches.

3.2. Introduction

Knowledge of where fluids are situated in a porous medium is fundamental to an understanding of how heterogeneity at the pore-scale leads to macroscale properties. This is applicable not only in hydrogeological contexts, but also across the whole range of porous systems of technological and scientific interest such as nanomaterials [1, 2] and biological systems [3, 4]. Many of the properties of interest are related to the complex interplay of liquid and gas within the pore space, and the resulting equilibrium distribution of phases contained therein [5, 6].

Given the ubiquity of the problem, several approaches have been used to calculate the phase distribution within a porous medium [7, 8], and we provide here only

a brief overview. Exact analytical solutions for capillary shape exist, but for only the simplest of systems (e.g., disks in two-dimensions) [9-16]. As the geometric complexity of the pore space increases, numerical approaches are needed, including continuum hydrodynamic modeling, lattice-Boltzmann method, molecular scale Monte Carlo simulation, and the Coarse-Grained Monte Carlo simulation methods discussed here.

Continuum hydrodynamic modeling of capillarity in a porous medium involves solving the Navier-Stokes equations subject to the geometrical boundary constraints of free interfaces and fixed surfaces, as well as the capillary forces in the system [17, 18] Systems are thus described by a second order partial differential boundary value problem, but the interfaces can suffer catastrophic events such as rupture or coalescence that need separate treatment [19]. As the size and geometric complexity of the system increases, so does the difficulty of numerically solving the associated equations.

Since interfaces arise from interactions between molecules, it is possible to use direct molecular simulation to capture phase distribution and interfacial geometry in a porous media. Molecular dynamics (MD) simulation would be most fundamental, and would at a larger scale, produce fluid flow consistent with continuum hydrodynamics. However, explicit evaluation of molecular motion for large complex pore spaces is prohibitive, both because of the cost of high spatial resolution and to capture realistic dynamics. A standard strategy for overcoming the cost of simulating exact molecular trajectories is to use the Monte Carlo method for molecular simulation, which can more directly and efficiently find local equilibrium configurations of molecules. It also naturally allows for simulating equilibrium adsorption/desorption from a reservoir via Grand

Canonical Monte Carlo, which is a standard method in molecular simulation to generate adsorption isotherms in porous materials such as zeolites [20]. As an additional step, fictitious but physically-motivated dynamics can be introduced via kinetic Monte Carlo [21] to mimic time evolution of the fluid system. However, atomistic Monte Carlo simulation is generally computationally limited to relatively simple pore geometries (e.g., Refs. [17, 22]), though advances in computing power and algorithms will continue to push the limits of feasibility [23].

Intermediate between the continuum and molecular models are coarse-grained models that sacrifice atomistic realism for computational efficiency while retaining the physically relevant pore-scale physics. Such methods become increasingly compelling as they present an opportunity to exploit the high-resolution pore space maps made available from advances in imaging, such as in X-ray micro computed tomography.

The lattice Boltzmann method [24], is such a coarse-grained model that retains hydrodynamic fluid transport, but via discrete Boltzmann equations representing particle collisions on a lattice. It has the advantage over continuum hydrodynamic modeling of not requiring special treatment of interfaces, which arise naturally from the interactions between particles in the bulk. This method has been used to compute properties associated with porous media [25], such as hydraulic conductivity. This methodology can be used with systems with complex pore space geometries, but carries a computational cost to capture the hydrodynamic transport, relative to Coarse-Grained Monte Carlo simulations.

Like the lattice Boltzmann method, Coarse-Grained Monte Carlo simulation coarse-grains many individual molecules into effective groups that reside on lattice sites

[26-29]. However, these lattice site groups contain information only of which phase is most prevalent at that location. No momentum information is retained, since to speed up determination of local phase equilibria, hydrodynamic behavior (which originates from momentum balance) is replaced by a more efficient stochastic dynamics. These lattice sites do interact through neighboring free-energetic interactions, and thus are capable of naturally capturing interfacial behavior. Just as molecular Monte Carlo simulation is an efficient alternative to molecular dynamics for molecular simulations, Coarse-Grained Monte Carlo is an efficient alternative to the lattice Boltzmann method for coarse-grained simulations of local equilibrium phase distributions.

It should be noted that the application of Coarse-Grained Monte Carlo to fluids in porous media involves a hypothesis that the local, metastable equilibria produced by the stochastic dynamics are representative of the experimental system. In many practical situations, the pore-scale capillary number, Ca = $\mu v/\gamma$, (where μ is the viscosity, v is the pore-scale velocity, and γ is the fluid/fluid interfacial tension) is small (e.g., oil trapped in pores of water-wet rock can typically have Ca ~ 10^{-6} - 10^{-4}) [30]. This corresponds to dominance of interfacial capillary stresses over viscous stresses (and usually inertial stresses as well given the low Reynolds numbers at these small length scales), and lends some argument for the quasistatic neglect of hydrodynamic transport in determination of local phase equilibria. There is also some support and analysis on the molecular scale for this hypothesis, where molecular Monte Carlo simulation has been verified to reproduce the hysteresis associated with such metastable states when compared with molecular dynamics simulations [31-33]. We present below direct validation of this hypothesis by comparison with experiment on natural porous media,

which has been previously lacking. In the following section, however, we first describe the Coarse-Grained Monte Carlo simulation algorithm, before reviewing and discussing its applications.

3.3. Coarse-Grained Monte Carlo Simulation Algorithm

The simulated system consists of a fixed solid porous medium, inside which several phases can exist. The system is represented by a lattice, with a resolution Δ represents the inter-lattice spacing chosen to adequately represent the pore-scale features of interest. Each lattice point (or cell) is assigned an identity corresponding to the majority phase at that point. To be concrete in the following discussion, we consider the case of a soil partially saturated with water, where there will be a total of three phases: solid (soil), water, and air (vapor). Each lattice point then is assigned to be one of these three phases, with the solid cells, representing the pore space geometry, fixed throughout the simulation, and the remaining cells corresponding to pore space that can be occupied with either water or air as the simulation proceeds. Following the convention for lattice gas models, we mathematically represent the phase of a lattice cell, *i*, by three occupation numbers, n_i , where α can take on the values of *s* (soil), *w* (water), or *a* (air). The occupation number n_i takes on the value 1 if lattice cell *i* is phase α, and 0 otherwise. The set of all occupation numbers for each lattice cell and each phase fully defines a configuration of the system.

The stochastic evolution of the system is governed by its total free energy

$$E = \sum_{i,j} J\, n_i\, n_j + \sum_i n_i^w \qquad (3.1)$$

where the first term on the right represents the sum of interaction free energies $J_{\alpha\beta}$ between neighboring lattice cells of phases α and β in contact, and the second term on the right is the sum of the chemical potential contributions μ for each cell occupied by water. (We take the zero of chemical potential to be that of the vapor phase; the chemical potential contribution of the solid is neglected since it is constant.) Note the first sum is over all nearest neighbor lattice cells *i* and *j*, while the second sum is over all phases for α and β, and the third sum is over all lattice cells *i*. The values of $J_{\alpha\beta}$ can be assigned based on experimental values γ for interfacial free energy according to the relation [34],

$$\gamma\Delta = 2J - T\ln\left[\coth\left(\frac{J}{T}\right)\right] \tag{3.2}$$

where *T* is the simulation temperature. This allows simulation parameters to be set in a manner that reflect the intrinsic properties concerning interfacial tension and/or contact angles (controlled by the ratio of interfacial tensions) from the interaction of real world materials.

The system is then updated from one configuration to the next by proposing a phase change in one or more cells, and then according to a specific criterion involving a random number, deciding whether to accept the proposed change or to reject it. Coarse-Grained Monte Carlo methods differ in the choice of which changes to propose. Algorithms that propose changes that conserves the total amount of each phase in the system are called "canonical", while those that regulate the total quantity of each phase by its chemical potential are called "grand canonical". Note that in canonical algorithms,

the chemical potential term in the total free energy is conventionally neglected, since it is constant as the total water content is fixed.

Coarse-Grained Monte Carlo methods also differ in the choice of the criterion for acceptance of a proposed update in configuration. Here we highlight the standard Metropolis algorithm, which serves as a common basis for several methods [35, 36]: accept the proposed change if $\exp(-\Delta E/k_B T)$ is greater than a random number chosen uniformly between 0 and 1, where ΔE is the change in total system energy for the proposed change in configuration and k_B is Boltzmann's constant. This algorithm is designed to drive the system towards thermodynamic equilibrium, at which point the probability of a given configuration is proportional to the Boltzmann factor, $\exp(-E/k_B T)$.

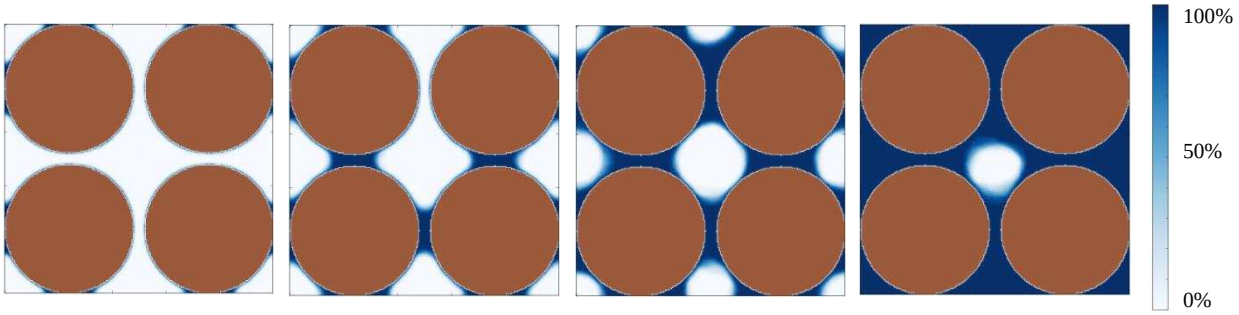

Figure 3.1: Canonical simulation result for four grains on a periodic 250x250 lattice grid at liquid water saturations from left to right of 10%, 25%, 50%, and 90%. The lowest saturation begins with the formation of the wetting layer and as saturation is increased capillary bridges are formed. At higher saturations the grains become fully wet with remaining air bubbles. The color bar at right shows the average density of the liquid.

Figure 3.1 shows the result of an illustrative example of a Coarse-Grained Monte Carlo simulation on a simple periodic system of 4 circular grains with varying water content. The canonical algorithm used here proposes new configurations with a liquid phase cell and a gas phase cell selected at random and swapped, and then accepts or rejects according to the Metropolis criterion. The values for $J_{\alpha\beta}$ are assigned as -1 for liquid/liquid, -2 for liquid/solid, and 1 for liquid/gas interactions, where the unit of energy

is taken to be k_BT. All other values are set to zero. These values correspond to perfect wetting and favor water adsorption onto the solid phase. The simulation is run for approximately 8,000 Monte Carlo time steps, where a time step is defined as N^2 attempted configuration changes (or moves), where N is the total number of lattice cells in the system. Equilibration to a point of less than 1% change in energy fluctuations typically occurs in about 1,500 time steps, with the remaining simulation time used for sampling.

3.4. Applications and Experimental Test

An early application of Coarse-Grained Monte Carlo simulation to solving for phase equilibria in porous materials of relatively simple geometries was the development of a Monte Carlo annealing method [26]. This approach sought to obtain the global energy minimum using three methods. The first and second methods for obtaining the energy minimum involved starting with either a fully wet or fully dry system and attempting to change individual lattice sites to a different phase (e.g. liquid to gas, or gas to liquid) one at a time until a global energy minimum was reached. The third approach used a Metropolis algorithm starting the system with a given level of liquid saturation and swapping liquid and gas phase cells. The system was evolved using Simulating Annealing, where the temperature was slowly lowered to approach the global minimum.

This method was adapted by [27] to applications in porous geologic material with the intent of using it to calculate thermal conductivity. The method was used to model fluid location within a complex geologic material. An example is shown in Figure 3.2.

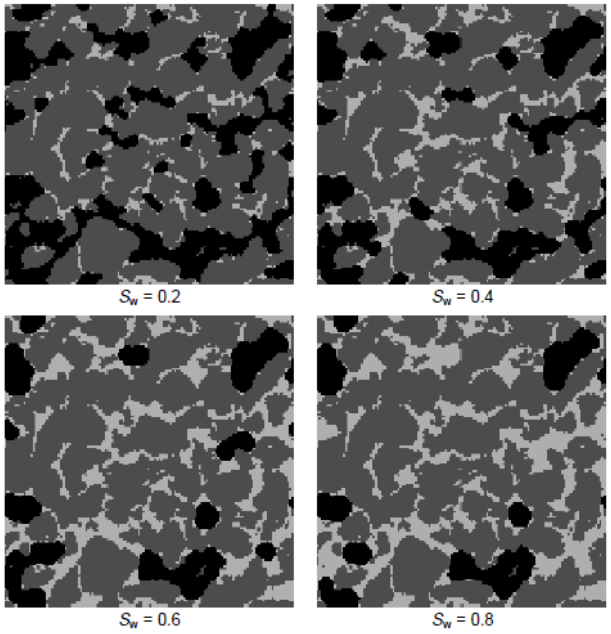

Figure 3.2: Fluid distribution result in a thin section of Berea sandstone. Dark gray represents rock, light gray is water, and black is air. The Sw values correspond to the level of saturation [27].

While the sandstone geometry was taken from a thin section, there was no experimental image including fluid location to validate against the simulation. After the multiphase equilibrium was established using the Monte Carlo annealing method, Fourier's law was used to calculate the thermal conductivity, showing qualitatively similar behavior as experiments at various moisture content. Interestingly they noticed a percolation behavior at the 40% water saturation level which is best explain by the water making its own thermally conductive pathway in addition to the rock phase to aid in the overall thermal conductivity.

Silverstein and Fort applied the Monte Carlo annealing method to random distributions of model particles [28, 37, 38]. The focus of the work was to calculate interfacial surface areas and hydraulic conductivity. To mimic continuous transport of the liquid phase, a canonical algorithm was employed where swaps are only attempted between liquid and gas cells a short distance apart. For interfacial surface area

calculations the systems were started as fully saturated with liquid cells removed that would provide the lowest interfacial free energy. Hydraulic conductivity functions and surface area calculations were carried out in both two and three dimensions. There were discrepancies at saturation levels below 50-60% when comparing the simulation results for interfacial area to experimental data. These were attributed to the experimental system not reaching the global energy minimum at low saturations, which is that generated by the Monte Carlo annealing method. Berkowitz & Hansen applied the Monte Carlo annealing method using pore space geometry data obtained from x-ray micro computed tomography of sandstone [39], but did not present experimental data to compare against.

Due to the importance of metastability, Lu et al. [29] employed a Coarse-Grained Monte Carlo simulation using the Metropolis algorithm directly at fixed simulation temperature, without simulated annealing. Because the simulation is coarse-grained in nature, interfacial energy is significantly greater than k_BT if the experimental temperature is used, and thus configurations are dominated by local energy minima. To address this, the simulation temperature T is assigned to a higher fictitious value that allows for sampling of all possible configurations while maintaining simulation efficiency. This requires the assumption that the distribution of stable and metastable energy minima is representative of that contained in a macroscopic sample. As the simulation proceeds, the system evolves through a series of metastable minima, trending towards equilibrium.

This modified method was applied to two-dimensional sections of an Ottawa sand system whose pore space was determined by X-ray micro computed tomography

[29]. The results were directly compared with experiments on the same systems. Results comparing the phase distribution as determined by experiment (top) and simulation (bottom) for various water saturations are shown in Figure 3.3.

The samples were prepared in small columns each containing a different amount of liquid saturation and then imaged at the Advanced Photon Source 13-BMD at Argonne National Laboratory. Two dimensional (2D) cross-sectional images were analyzed to extract the grain and pore space data from samples containing 15%, 25%, 70%, and 90% liquid saturation. These images are represented in Figures 3.3a-3.3d. The grain and pore space data were discretized into a lattice and MC simulation was carried out with similar saturation conditions. These results are given in Figures 3.3e-3.3h. The comparison between experiment (Figures 3.3a-3.3d) and simulation (Figures 3.3e-3.3h) shows similar distributions of adsorbed water in the pore space. Under low saturation conditions, liquid is condensed within many of the smaller pores in the system. At higher saturations the water is also adsorbed in the same locations but perhaps what is more remarkable is the similarity in the shape of the gas “bubble”, particularly evident at the 90% saturation level.

Lu et al. also presented a method for calculating the capillary pressure, ΔP, as a function of water content, an important quantity in soil mechanics referred to as the soil-water retention curve (SWRC). Capillary pressure is calculated by measuring the radius of curvature, r, of individual interfaces found in the simulation, and using the Young-Laplace equation for the pressure difference across the liquid-vapor interface, $P = \frac{2}{r}$.

As a result of running simulations in two dimensions, an assumption is made that the two principle radii of curvature are equal to the one observed in the two-dimensional

configuration. The result is given in Figure 3.3i. The simulation SWRC agrees with the experimental SWRC (prepared by the conventional Tempe cell method [6]) with deviations of less than 8%. Thus the simulation methodology can accurately capture quantitative properties of complex porous materials.

3.5. Grand Canonical Monte Carlo Simulation for Wetting/Drying Hysteresis

As porous materials are exposed to either wetting or drying conditions, liquid flows into or out of the material. Properties thus follow a hysteretic, i.e. path-dependent, trajectory, and depend on whether conditions are wetting or drying. The primary reason we see hysteresis in simulation is because of the metastability of local equilibrium interfacial configurations in the pore space. This series of metastable configurations is difficult to characterize or predict in a complex pore space. To isolate the effects and principles behind the hysteresis, many studies on adsorption hysteresis have been carried out on simple pore geometries, and not generally on experimentally determined pore spaces. Woo et al. did carry out a Coarse-Grained Grand Canonical Monte Carlo simulation in a random pore space with statistical properties similar to Vycor glass [40]. This was mainly to compare the adsorption hysteresis to a mean-field treatment, concluding that the hysteresis behavior was controlled largely by metastable configurations. Below, we present grand-canonical Coarse-Grained Monte Carlo simulation performed on an experimentally determined pore space.

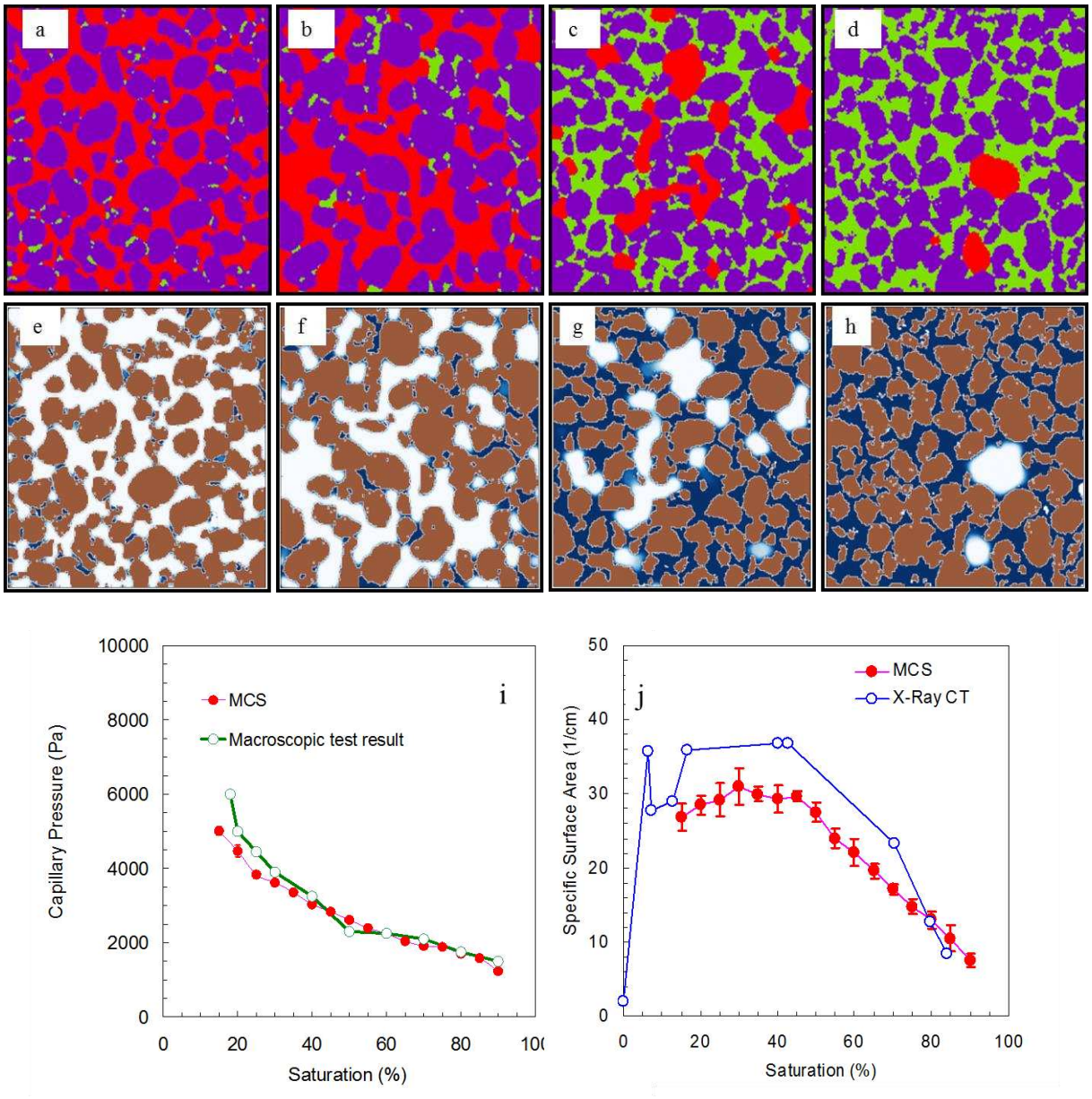

Figure 3.3: Results for a three phase study of capillarity in Ottawa sand. (a)-(d) show microXCT images of partially wet Ottawa sand with solid represented as purple, gas as red, and liquid as green. Image size is 3.521mm x 3.521mm. From left to right, the liquid saturation is 15%, 25%, 70%, 90%. (e)-(h) show Monte Carlo simulation (MCS) output for identical pore spaces with the same liquid saturations, with solid as brown, gas as white, and liquid as blue. Simulation resolution is 250 lattice units x 250 lattice units with an interlace unit spacing of 10.06 microns. (i) shows the soil-water retention curve comparison between simulation and macroscopic experiment. (j) shows the capillary specific surface area between simulation and experiment [29].

In grand-canonical Coarse-Grained Monte Carlo, the algorithm for proposing a change in system configuration consists simply of picking a pore space cell at random and changing the phase from water to air or vice versa. The rest of the algorithm proceeds without modification. A higher chemical potential drives the system to lose water, while a lower chemical potential drives the system to gain water. The result is that the simulation functions similarly to experimental adsorption/desorption experiments where adsorbate is driven to adsorb/desorb on a material using a pressure gradient. The chemical potential here functions analogously to the pressure gradient in experiment, and can be related via the equation of state. For a simulation under wetting conditions, the cells in the pore space are all initially assigned as air, i.e., 0% liquid saturation. For drying conditions, the pore space cells are initially all set to liquid, corresponding to 100% saturation.

Figure 3.4 shows the wetting/drying hysteresis in simulations carried out on a system of randomly distributed circular disks. The distribution of these circular disks corresponds to a two-dimensional slice of an X-ray micro computed tomography image taken of a sample consisting of 400-600 µm glass beads. As before, we use a simulation temperature corresponding to $k_BT = 1$. Simulation output for chemical potentials ranging from 2.1-2.45 (also in units of k_BT) is shown in Figure 3.4. Figure 3.4a-3.4b shows the phase distribution under drying conditions while Figure 3.4c-3.4d shows that corresponding to wetting conditions. The degree of hysteresis in water content in these figures is generally consistent with that seen in experiment.

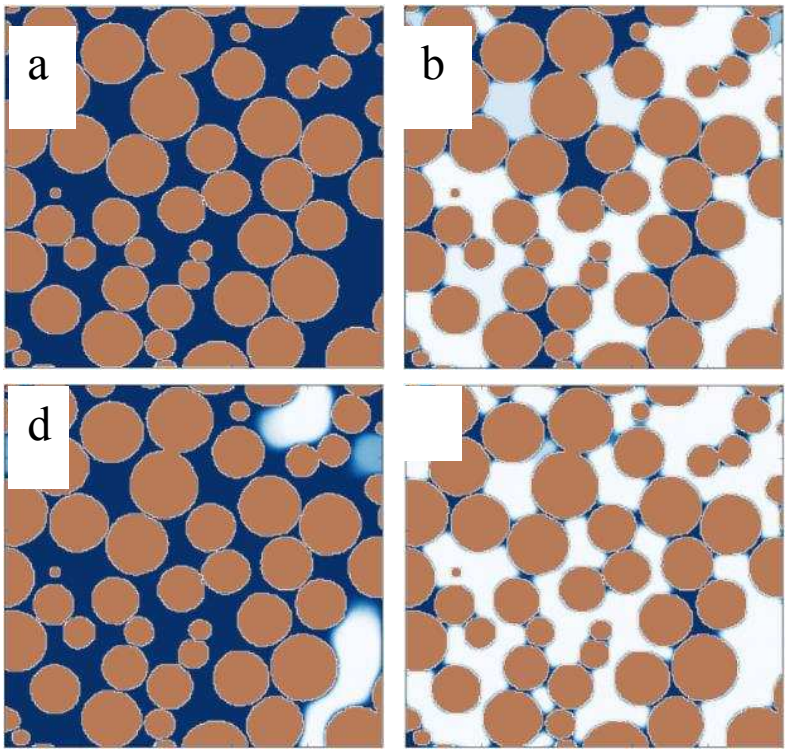

Figure 3.4: Simulation output showing water distributions at chemical potential values of 2.1 and 2.45 (from left to right). Drying is shown in panels (a)→(b), and wetting in panels (c)→(d). Notice that despite having the same chemical potential value, the resulting capillary distributions are quite different between the wetting and drying cases.

3.6 Conclusions

Coarse-Grained Monte Carlo simulation is an effective tool for the study of phase distribution in porous materials. By coarse graining the system to a lattice and eliminating the computational overhead involved in calculating hydrodynamic flows, the simulation methodology can be used to calculate constitutive properties of these materials in a highly efficient manner. Approaches in the literature are diverse and in the case of adsorption phenomena tend to focus on molecular simulation and simplified model single-pore systems. The Coarse-Grained Monte Carlo simulation can make direct correspondence with experimental systems, by using pore space geometries from experimental imaging

techniques (e.g. X-ray micro computed tomography) and interfacial coupling parameters from experimentally determined surface tensions.

By performing simulations and experiments on the same pore spaces, we have presented here direct validation of the Coarse-Grained Monte Carlo simulation methodology. Simulation results conform well with experimental data, particularly in the case of capillarity in soils in the equilibrium phase distribution, soil-water retention, and capillary specific surface area. We introduced a method to use a two-dimensional slice of the three-dimensional pore space to model constitutive properties, at a great savings in computational cost. We furthermore have shown that Coarse-Grained Monte Carlo generates metastable configurations that are representative of those seen in experiment, as previously hypothesized based on molecular simulation results and supported by quasistatic arguments about the dominance at the pore scale of capillary forces over hydrodynamic forces for typical conditions. This supports our approach of using a fixed simulation temperature in Coarse-Grained Monte Carlo rather than using Simulated Annealing as in prior methods.

3.7 References Cited

[1] A. Striolo, “Water self-diffusion through narrow oxygenated carbon nanotubes,” *Nanotechnology*, vol. 18, no. 47, p. 475704, Nov. 2007.

[2] G. M. Torrie, G. Lakatos, and G. N. Patey, “Structure and adsorption of water in nonuniform cylindrical nanopores.,” *J. Chem. Phys.*, vol. 133, no. 22, p. 224703, Dec. 2010.

[3] S. J. Pogorzelski, Z. Berezowski, P. Rochowski, and J. Szurkowski, “A novel methodology based on contact angle hysteresis approach for surface changes monitoring in model PMMA-Corega Tabs system,” *Appl. Surf. Sci.*, vol. 258, no. 8, pp. 3652–3658, Feb. 2012.

[4] M. R. Urist, “Bone: Formation by Autoinduction,” *Science (80-.).*, vol. 150, no.

3698, pp. 893–899, Nov. 1965.

[5] P.-G. de Gennes, F. Brochard-Wyart, and D. Quere, *Capillarity and Wetting Phenomena: Drops, Bubbles, Pearls, Waves (Google eBook)*. Springer, 2004.

[6] N. Lu and W. J. Likos, *Unsaturated Soil Mechanics*. Wiley, 2004.

[7] P. Meakin and A. M. Tartakovsky, “Modeling and simulation of pore-scale multiphase fluid flow and reactive transport in fractured and porous media,” *Rev. Geophys.*, vol. 47, no. 3, p. RG3002, Jul. 2009.

[8] D. W. Siderius and L. D. Gelb, “Predicting gas adsorption in complex microporous and mesoporous materials using a new density functional theory of finely discretized lattice fluids.,” *Langmuir*, vol. 25, no. 3, pp. 1296–9, Feb. 2009.

[9] R. A. Fisher, “On the capillary forces in an ideal soil; correction of formulae given by W. B. Haines,” *J. Agric. Sci*, vol. 16, p. 492, 1926.

[10] Z. Grof, C. J. Lawrence, and F. Štěpánek, “The strength of liquid bridges in random granular materials,” *J. Colloid Interface Sci.*, vol. 319, no. 1, pp. 182–192, 2008.

[11] T. Gröger, U. Tüzün, and D. M. Heyes, “Modelling and measuring of cohesion in wet granular materials,” *Powder Technol.*, vol. 133, no. 1, pp. 203–215, 2003.

[12] J. Lechman and N. Lu, “Capillary Force and Water Retention between Two Uneven-Sized Particles,” *J. Eng. Mech.*, vol. 134, no. 5, pp. 374–384, May 2008.

[13] G. Mason and W. C. Clark, “Liquid bridges between spheres,” *Chem. Eng. Sci.*, vol. 20, no. 10, pp. 859–866, 1965.

[14] F. M. Orr, L. E. Scriven, and A. P. Rivas, “Pendular rings between solids: meniscus properties and capillary force,” *J. Fluid Mech.*, vol. 67, no. 04, p. 723, Mar. 2006.

[15] P. Pierrat and H. S. Caram, “Tensile strength of wet granula materials,” *Powder Technol.*, vol. 91, no. 2, pp. 83–93, 1997.

[16] V. Richefeu, M. El Youssoufi, and F. Radjaï, “Shear strength properties of wet granular materials,” *Phys. Rev. E*, vol. 73, no. 5, p. 051304, May 2006.

[17] C. Cuvelier and R. M. S. M. Schulkes, “Some Numerical Methods for the Computation of Capillary Free Boundaries Governed by the Navier–Stokes Equations,” *SIAM Rev.*, vol. 32, no. 3, pp. 355–423, Sep. 1990.

[18] Y. D. Shikhmurzaev, *Capillary Flows with Forming Interfaces*. CRC Press, 2007.

[19] A. Q. Raeini, M. J. Blunt, and B. Bijeljic, “Modelling two-phase flow in porous media at the pore scale using the volume-of-fluid method,” *J. Comput. Phys.*, vol. 231, no. 17, pp. 5653–5668, Jul. 2012.

[20] D. Frenkel and B. Smit, *Understanding Molecular Simulation: From Algorithms to Applications*. Academic Press, 2001.

[21] R. Ziff, E. Gulari, and Y. Barshad, “Kinetic Phase Transitions in an Irreversible Surface-Reaction Model,” *Phys. Rev. Lett.*, vol. 56, no. 24, pp. 2553–2556, Jun. 1986.

[22] J.C. Liu and P. A. Monson, “Molecular Modeling of Adsorption in Activated Carbon: Comparison of Monte Carlo Simulations with Experiment,” *Adsorption*, vol. 11, no. 1, pp. 5–13, Jan. 2005.

[23] J. Kim and B. Smit, “Efficient Monte Carlo Simulations of Gas Molecules Inside Porous Materials.,” *J. Chem. Theory Comput.*, vol. 8, no. 7, pp. 2336–43, Jul. 2012.

[24] S. Chen and G. D. Doolen, “Lattice Boltzmann Method for Fluid Flows,” *Annu. Rev. Fluid Mech.*, vol. 30, no. 1, pp. 329–364, Jan. 1998.

[25] M. E. Kutay, A. H. Aydilek, E. Masad, and T. Harman, “Computational and experimental evaluation of hydraulic conductivity anisotropy in hot-mix asphalt,” *Int. J. Pavement Eng.*, vol. 8, no. 1, pp. 29–43, Mar. 2007.

[26] R. Knight, A. Chapman, and M. Knoll, “Numerical modeling of microscopic fluid distribution in porous media,” no. September 1989, pp. 994–1001, 1990.

[27] S. Mohanty, “Effect of multiphase fluid saturation on the thermal conductivity of geologic media,” *J. Phys. D. Appl. Phys.*, vol. 30, no. 24, pp. L80–L84, Dec. 1997.

[28] D. L. Silverstein and T. Fort, “Incorporating Low Hydraulic Conductivity in a Numerical Model for Predicting Air−Water Interfacial Area in Wet Unsaturated Particulate Porous Media,” *Langmuir*, vol. 16, no. 2, pp. 835–838, Jan. 2000.

[29] N. Lu, B. D. Zeidman, M. T. Lusk, C. S. Willson, and D. T. Wu, “A Monte Carlo paradigm for capillarity in porous media,” *Geophys. Res. Lett.*, vol. 37, no. 23, Dec. 2010.

[30] A. Cense and S. Berg, “The viscous-capillary paradox in 2-phase flow in porous media,” *Int. Symp. Soc.,* 2009.

[31] L. Sarkisov and P. A. Monson, “Hysteresis in Monte Carlo and Molecular Dynamics Simulations of Adsorption in Porous Materials,” *Langmuir*, vol. 16, no. 25, pp. 9857–9860, Dec. 2000.

[32] L. Sarkisov and P. A. Monson, “Modeling of Adsorption and Desorption in Pores of Simple Geometry Using Molecular Dynamics,” *Langmuir*, vol. 17, no. 24, pp. 7600–7604, Nov. 2001.

[33] P. A. Monson, “Understanding adsorption/desorption hysteresis for fluids in mesoporous materials using simple molecular models and classical density functional theory,” *Microporous Mesoporous Mater.*, vol. 160, pp. 47–66, Sep. 2012.

[34] L. Onsager, “Crystal Statistics. I. A Two-Dimensional Model with an Order-Disorder Transition,” *Phys. Rev.*, vol. 65, no. 3–4, pp. 117–149, Feb. 1944.

[35] N. Metropolis, A. W. Rosenbluth, M. N. Rosenbluth, A. H. Teller, and E. Teller, “Equation of State Calculations by Fast Computing Machines,” *J. Chem. Phys.*, vol. 21, no. 6, p. 1087, Dec. 1953.

[36] K. Binder, “Monte Carlo calculation of the surface tension for two- and three-dimensional lattice-gas models,” Phys. Rev. A, vol. 25, no. 3, pp. 1699–1709, Mar. 1982.

[37] D. P. Laundau and K. Binder, *A Guide To Monte Carlo Simulations In Statistical Physics*. Cambridge University Press, 2005.

[38] D. L. Silverstein and T. Fort, “Prediction of Water Configuration in Wet Unsaturated Porous Media,” *Langmuir*, vol. 16, no. 2, pp. 839–844, Jan. 2000.

[39] B. Berkowitz and D. P. Hansen, “A Numerical Study of the Distribution of Water in Partially Saturated Porous Rock,” *Transp. Porous Media*, vol. 45, no. 2, pp. 301–317.

[40] H.J. Woo, F. Porcheron, and P. A. Monson, “Modeling desorption of fluids from disordered mesoporous materials.,” *Langmuir*, vol. 20, no. 11, pp. 4743–7, May 2004.

CHAPTER 4

A Monte Carlo Paradigm for Capillarity in Porous Media

A Paper published in Geophysical Research Letters[1]

Ning Lu[2], Benjamin D Zeidman[3], Mark T. Lusk[4], Clinton Willson[5], and David T. Wu[6]

4.1. Abstract

Wet porous media are ubiquitous in nature as soils, rocks, plants, and bones, and in engineering settings such as oil production, ground stability, filtration and composites. Their physical and chemical behavior is governed by the distribution of liquid and interfaces between phases. Characterization of the interfacial distribution is mostly based on macroscopic experiments, aided by empirical formulae. We present an alternative computational paradigm utilizing a Monte Carlo algorithm to simulate interfaces in complex realistic pore geometries. The method agrees with analytical solutions available only for idealized pore geometries, and is in quantitative agreement with micro X-ray CT, capillary pressure and interfacial area measurements for natural soils. We demonstrate that this methodology predicts macroscopic properties such as the capillary pressure and air-liquid interface area versus liquid saturation based only on

---

[1] Reprinted with Permission of Geophysical Research Letters: N. Lu, B. D. Zeidman, M. T. Lusk, C. S. Willson, and D. T. Wu, “A Monte Carlo paradigm for capillarity in porous media,” *Geophys. Res. Lett.*, vol. 37, no. 23, Dec. 2010.

[2] Primary author, Department of Civil and Environmental Engineering, Colorado School of Mines.

[3] Graduate student and primary researcher, Department of Chemistry and Geochemistry, Colorado School of Mines.

[4] Department of Physics, Colorado School of Mines.

[5] Department of Civil and Environmental Engineering, Louisiana State University.

[6] Department of Chemistry and Geochemistry, Colorado School of Mines.

the pore size information from microXCT images. The generality of this method should allow simulation of capillarity in many porous materials.

4.2. Introduction

Capillary phenomena in porous media involve an intricate interplay of liquid, solid, and gas [1]. The interfacial geometries that separate phases are often complicated and are dictated by intermolecular forces, pore structure, pressure and temperature [2]. At the pore scale, analytical techniques are generally confined to solutions of the Laplace-Young equation for idealized particle geometries such as spheres or disks [3-10]. While such solutions give important physical insights, the need remains for a methodology to address more complicated pore geometries such as in soils [11,12], and plant tissue [13]. Monte Carlo (MC) simulation, and the related lattice-gas and lattice-Boltzmann techniques that account for coarse-grained transport, can in principle incorporate the fundamental physical interactions in more complex geometries. Several recent studies have carried out MC simulations of capillarity at the molecular and nanometer scale in pores. However, these systems are strongly influenced by thermal fluctuations and have also focused on simple pore geometries such as slits and cylinders [14-19]. Furthermore, such microscopic approaches must be scaled-up to predict macroscopic properties of a composite. Computational fluid dynamics and lattice gas automata methods have been used to compute the pore-scale geometrical evolution of liquid bodies in porous media with complex pore geometries, but with the computational overhead of capturing the transport behavior [20]. There has also recently been a coarse-grained approach based on direct discretized simulation of the

liquid-vapor interface directly, although this introduces complications associated with the merging and breakup of liquid domains [9].

4.3. Methodology

To address the need for an efficient pore-scale simulation methodology we developed a coarse-grained Monte Carlo lattice gas approach. This simulation methodology is capable of efficiently ascertaining the phase distribution and interface equilibria found in porous materials with complex geometrical arrangements. To illustrate these abilities we chose several granular pore systems with increasing geometric complexity: Two spherical grains in contact (for which exact solutions to the Young-Laplace equation are possible), spherical grains of differing sizes arranged randomly, and the grain configuration for a real-world Ottawa sand sample. The multiphase nature of these systems is thus treated as a three-spin Ising model where the spins correspond to the different phases: solid, liquid, and gas. Initial simulation conditions were set by discretizing the granular and pore-space domains onto the lattice. These solid phase domains remain fixed. Next, a liquid phase is introduced in the pore space at random lattice points corresponding to the amount of liquid saturation we wish to simulate. An interfacial free energy of contact between the lattice points, $J_{\alpha\beta}$, is determined between cells of differing types α and β [21]. The (free) energy of the system can be written as

$$E = \sum_{i,j} \sum_{\alpha,\beta} J_{\alpha\beta} n_i^{\alpha} n_j^{\beta} \tag{4.1}$$

where the first sum is over all nearest neighbor cells i and j, the second sum is over all phases, and $n_i^{\alpha} = 1$ if cell i is in phase α and 0 otherwise. The liquid and gas phases

are then evolved according to the standard Metropolis algorithm where the probability of a given configuration is proportional to the Boltzmann factor, $\exp(-E / kT)$, with k being Boltzmann's constant and T the temperature. Due to the coarse grained nature of simulation, the interfacial energy is much greater than kT and configurations are dominated by local energy minima separated by the energy barriers. To allow for efficient sampling, we chose a fictitious higher value for the temperature that allows exploration of all possible configurations while still being low enough to be dominated by the (free) energy minima. We assume that the distribution of stable and metastable energy minima sampled is representative of that in a macroscopic sample. In this limit, the (ratios of) interfacial free energies serve to set the contact angles between phases. The interfacial tension in a lattice gas can in principle depend on the angle of the interface relative to the lattice vectors. However, for the square lattice used here, the dependence is weak, and the interfaces do not noticeably deviate from the circular shape predicted by an angle-independent interfacial tension. This minor effect might be further reduced by going to a more symmetric lattice, such as the hexagonal lattice. Furthermore, in the limit of perfect wetting, the contact angle becomes insensitive to the free energy ratio, and values of J can be chosen so as to reproduce (near) perfect wetting. To satisfy this criterion, the interfacial free energies per unit area were assigned as follows: -1 for liquid/liquid, 1 for liquid/gas, and -2 for liquid/solid interaction. Zero was assigned to all other interaction values. These otherwise arbitrary values were chosen to favor adsorption and wetting of liquid onto the solid phase. The unit of energy is taken to be kT throughout.

4.4. Validation

A simple geometry consisting of two disks of radius *R* in contact, shown in Figure 4.1, was used to compare the MC approach with the classical solution based on the Laplace-Young equation for different liquid contents. Figure 4.1I shows typical equilibrations of the energy for a range of liquid saturations. Systems with higher liquid content require more MC steps to reach equilibrium (though all simulations were carried out for much longer than shown in these plots). The two-dimensional Laplace-Young equation predicts that the liquid-vapor interface in the region between the disks is a circular arc, which is well-captured by the MC simulation. For the present case of zero contact angle, the theoretical radius of curvature is $r = R\left(\frac{1}{\cos\theta} - 1\right)$, where the filling angle θ, depicted in Fig. 4.1A, is defined to be the angle between the contact point between the disks and the three-phase contact point [3, 24]. A least-squares circular fit was performed on the averaged equilibrated profiles to extract a radius of curvature and filling angle for the simulation results shown in Fig. 4.1A-H. Fig. 4.1J compares the theoretical and simulated radii of curvature. In general, the MC results accord well with analytical predictions but systematically estimate a smaller radius of curvature. This difference, which is less than 4%, can be attributed to the neglect in the analytical model of surface hydration on the solid, an effect known to play a role in surface adsorption phenomena. The disparity increases slightly with liquid content (Fig. 4.1J), a trend seen in the thickness of the layer of liquid condensation (Fig 4.1A-H).

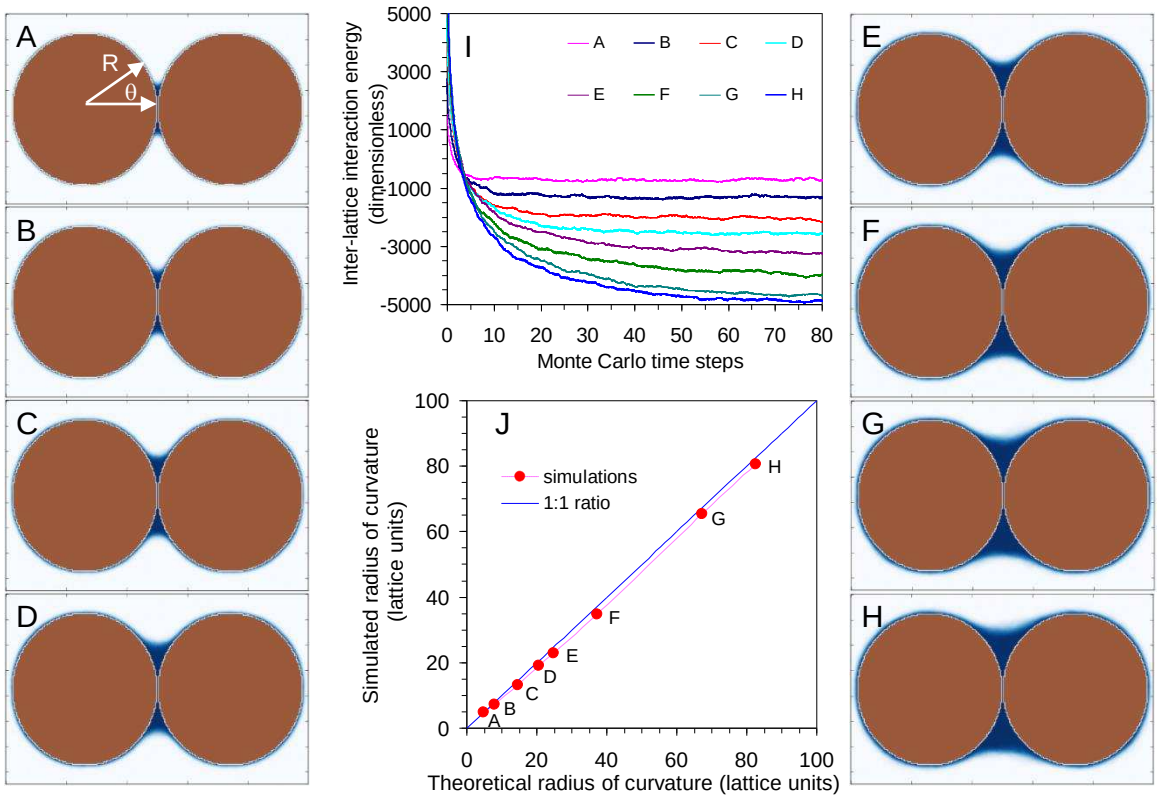

Figure 4.1: Configurations of capillary condensation between two disks (brown) for varying liquid fractions. Simulations were run in a 250 × 150 lattice grid for ~11,000 MC steps with periodic boundary conditions. Equilibrium was assumed when the standard deviation normalized with respect to the total system energy (eq. (1)) was less than 1% as shown in Fig. 1I. After equilibration, ~200 frames taken every 32 MC steps were averaged to create a density profile for the liquid. The air-liquid interface was chosen to be the 50% density contour. As illustrated in Fig. 1J, least-squares circular fits of this contour permitted calculation of various interfacial properties, including the radius of curvature and contact angle, that were compared with theory. The circular disks are 125 lattice units in diameter. The filling angle θ, depicted in (A), describes the liquid fraction. Simulated interface configurations are for (A) θ = 22.5º, (B) θ = 28.1º, (C) θ = 36.6º, (D) θ = 42.0º, (E) θ = 45.0º, (F) θ = 51.9º, (G) θ = 61.9º, and (H) θ = 65.1º.

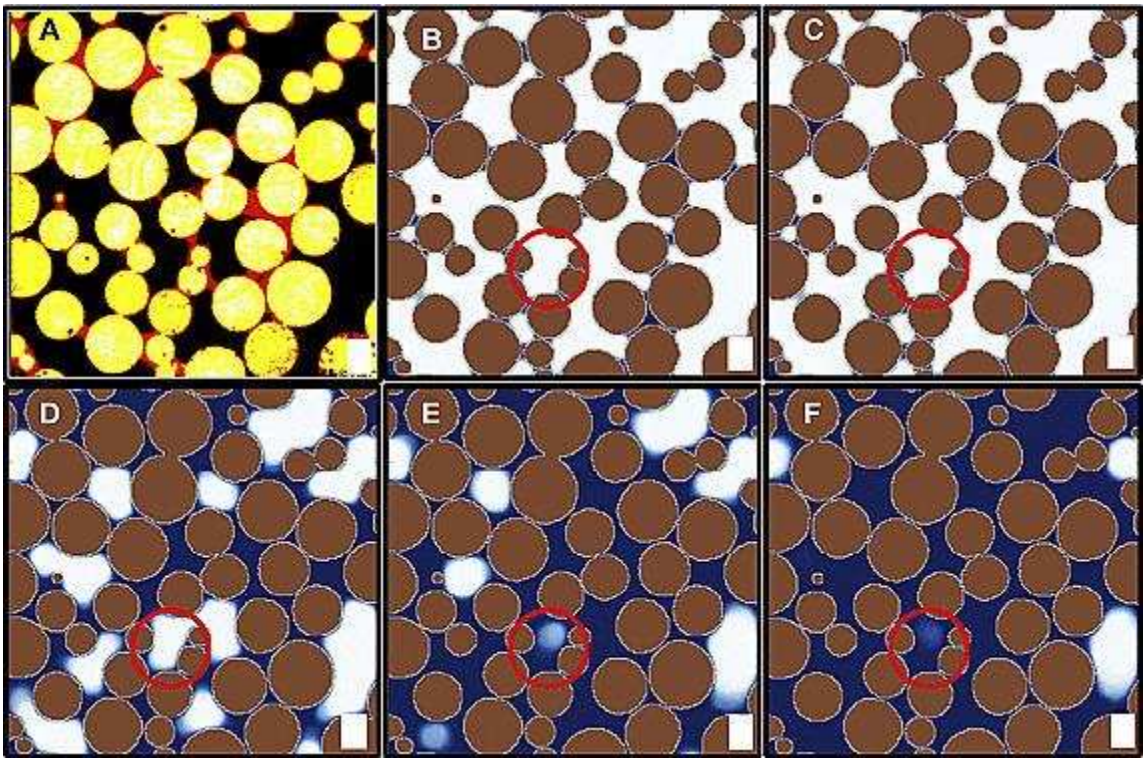

Figure 4.2: (A) X-Ray MicroCT image of a planar cross-section of wet randomly sized and distributed glass beads (400-600 microns in diameter). Air is shown in black, liquid water in red, and glass beads in yellow. The water is doped by 4% of CsCl to distinguish soil from water. The expirement did contain glass beads of differing chemical composition and wettability resulting in a different x-ray adsorption coefficient across the range of x-ray energies used. Since the goal was to use this setup to validate simulation in a geometrically complex pore system these differing wettabilites were ignored. They can however be easily taken into account by the simulation by defining the different beads as separate solid phases with their own interaction parameters. Simulations on systems with differing wettability are planned for future work. Each image has dimensions of 2.59 mm × 2.59 mm and a pixel resolution of 7.4 microns. (B)-(F) Simulation (in 250 × 250 lattice grid) snapshots at various liquid contents using the same locations for the solid grains. Air is shown in white, liquid water in blue, and glass beads in brown. Red circles illustrate regions where phase change is sensitive to changes in total water saturation.

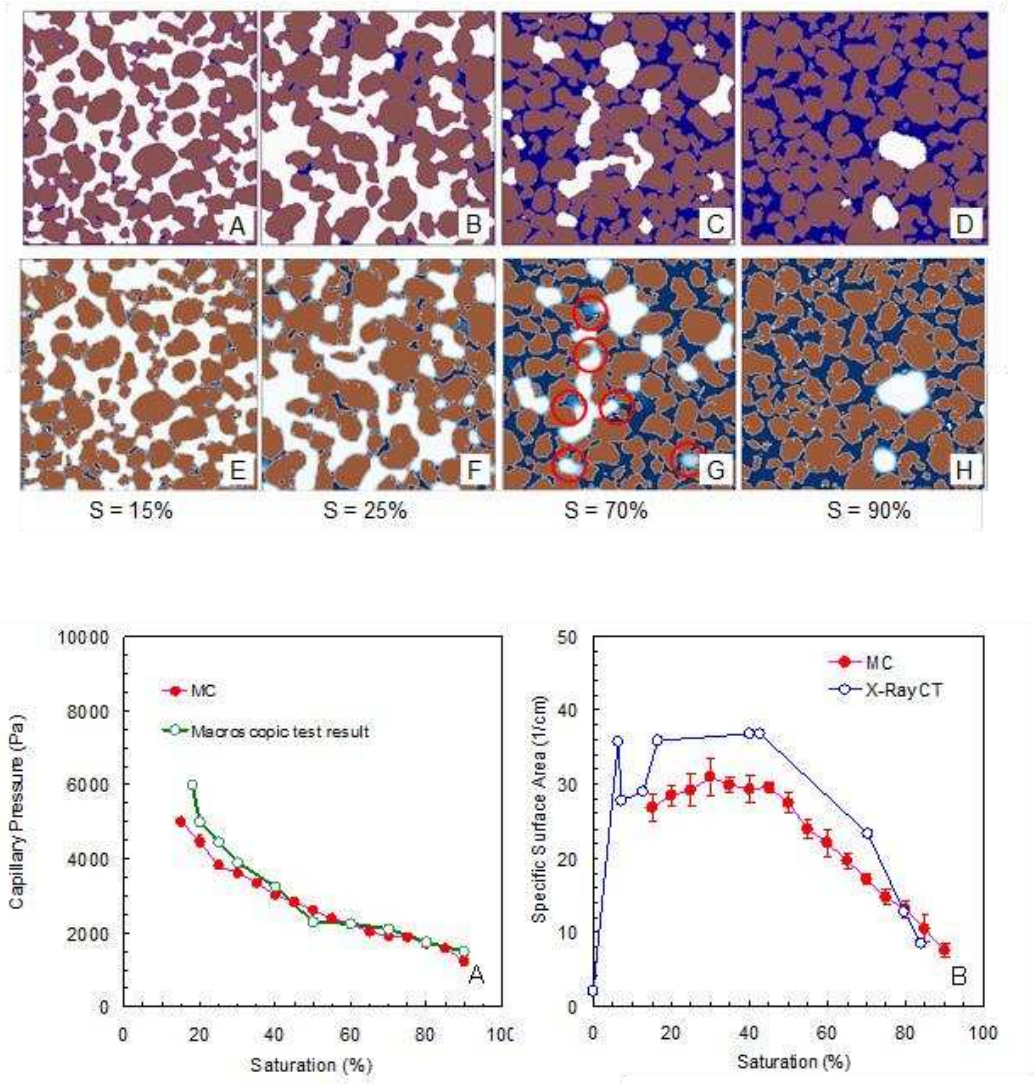

Figure 4.3: (A)-(H) comparisons of liquid retention for Ottawa sand between the microXCT images and MC simulations. The top row shows the microXCT images with solid in brown, liquid in blue, and gas in white colors under different liquid saturations. The second row shows the MC simulation (in 250 × 250 lattice grid) results with the grain positions taken from the microXCT images under different liquid saturations. Each image has dimensions of 3.521 mm × 3.521 mm and has a pixel resolution of 10.06 microns. The water is doped by 6% of CsCl to distinguish soil from water. Red circles illustrate regions where phase change is sensitive to changes in total water saturation. (I) comparison of the capillary pressure-saturation curve from macroscopic laboratory experiments and the calculated capillary pressure-saturation curve from MC simulation, and (J) comparison of calculated specific air-liquid interface area curve from 2D cross-sections of microXCT images and the specific air-liquid interface area curve from MC simulation. The MC curve was calculated by measuring individual principal radii through the least-squares fitting method and determining the average capillary pressure for a given saturation.

Further validation of the MC methodology on a more complex geometry was obtained through comparisons with experimental images for assemblies of randomly sized and distributed glass beads of size 400-600 μm. Fig. 4.2 compares a Micro X-ray Computed Tomography (microXCT) image showing water distributions (Fig. 2A), with simulations of the same system (Fig. 4.2B-F) under different water saturations. For much of the sample, the simulated menisci shown in Fig. 4.2C (at 25% saturation) match the bridging patterns seen in the microXCT image in Fig. 4.2A. The few differences are mainly between particles farther apart and may reflect hysteresis between metastable water distributions associated with complex granular packings. In fact, multiple simulations and experiments on the same initial grain configurations yield slightly different equilibrated capillary bridging; nevertheless, interstitial pore spaces contain similar amounts and shapes of water.

4.5. Application to Capillarity in Soils

The MC methodology was next used to model the distribution of water in a more realistic sample of soil, one of the most abundant and complex porous materials. Ottawa sand was prepared with different liquid saturations and X-Ray computed-tomography images were obtained for each case. Representative two-dimensional (2D) cross-sectional images (Fig. 4.3A-4.3D) of the grain and pore structure were extracted from the 3D image and then used in the MC analyses. We conducted simulations for each of these 2D configurations by varying liquid saturation from dry to completely wet. The results for each configuration at the same saturations as the experimental data (Fig. 4.3A-4.3D), are shown in Fig. 4.3E-4.3H. The distributions of liquid water are remarkably similar between the X-Ray images and MC predictions.

Having validated the MC approach, we now turn to its application in developing macroscopic constitutive relations. In particular, we focus on the relation between liquid saturation and capillary pressure, P, an important material property governing liquid retention, inter-granular forces, and fluid flow in porous materials. For porous media such as soil, the relation is often referred to as the adsorption isotherm or soil-water retention curve (SWRC) [22,23]. The SWRC is typically constructed by fitting macroscopic experiments to an empirical equation. Here we offer a theoretical way to compute the SWRC employing the Laplace-Young equation, where r is the average principal radius of curvature obtained from the local liquid-vapor interfaces [23]. The factor of two in the equation is associated with the conversion of 2D images to 3D. All simulations shown in this paper were performed in two-dimensions. In 3D the Young-Laplace equation takes into account a second principal radius of curvature. Since this value does not exist in the 2D equation, an inherent discrepancy between 2D and 3D calculations in this model exists. By analytically solving for the SWRC for a simple cubic packing in both 2D and 3D it can be shown that the 2D SWRC is approximately a factor of two in magnitude less than that of the 3D SWRC. This factor of two also results if one approximates the interfaces as spherical. This approximate scaling factor of 2 was used in the calculations presented here to relate the 2D Monte Carlo results to 3D systems. Ts is the surface tension of water: 71.79 dyn/cm at 25℃. The experimental SWRCs for t he four different saturations (Fig. 4.3A-D) compare favorably with those from MC simulation performed on grain positions given by the microXCT images (Fig. 4.3E-H). This is shown in Fig. 4.3I, and the relative differences are less than 8%. These results confirm that the MC approach

represents a new quantitative means for both understanding and predicting properties resulting from the intricate interfacial interactions of complex porous materials.

A second important macroscopic relation is the relation between the air-liquid interfacial area and liquid saturation, often referred to as the specific surface area curve (SSAC). The SSAC characterizes, for instance, the composite tensile strength and can be used to predict trends in the rates of biological activities [e.g., Nichols et al., 2005]. It can be readily obtained from our MC analysis by counting the number of air-water lattice contacts for clusters of water, multiplied by the length of a lattice unit and normalized by the total simulation area. Figure 4B compares results from microXCT and MC predictions. For this soil, the specific surface area peaks between 30 and 37 cm-1 for saturation between 30 and 50%. The overall patterns between the SSACs from the two methods show excellent qualitative agreement, and differ by less than 20%. Some of this is due to the resolution of both techniques, more pronounced for the microXCT images when liquid saturation is low. The current resolution for the microXCT imaging is around 10 □m. The SSAC, a non-monotonic function of liquid saturation, governs the mechanical behavior of wet soil. The tensile strength of wet granular materials as a function of liquid saturation has been investigated for many years [4,7,11,12]. Yet a theory that describes tensile strength for all saturations has been developed only recently [24]. The theory leads to a closed form analytical equation for tensile strength under all saturations and predicts the same non-monotonic behavior shown in Fig. 4.3J for sandy soils, strongly indicating that the SSAC of the liquid-air interface plays a dominant role in the tensile strength of wet granular media. The MC approach provides a direct link between liquid saturation and tensile strength.

4.6. Discussion

Since the MC simulation is coarse-grained in lattice units, the SWRC and SSAC results can be scaled up by simply changing the lattice cell size. For example, if the dimensions of the simulation region shown in Fig. 4.3A-H is 1/100th of the 3.521 mm × 3.521 mm cell used for Ottawa sand, a typical scale for silty soil, and if the relative pore distribution remains the same, the corresponding capillary pressure and specific liquid-air interface area curves in Fig. 4.3I-J would be simply multiplied by a factor of 100. A profound implication is that once the pore structures and pore material compositions are determined by high resolution imaging techniques such as microXCT, SEM, and TEM, the associated multi-phase and interfacial properties such as adsorption isotherms and specific surface area curves can now be computed without expensive and time-consuming macroscopic experiments.

The MC methodology is thus a computationally innovative approach to quantify important structural and macroscopic constitutive relations in wet porous media. The cases above focus only on homogeneous materials, however it is straightforward to simulate regions wherein saturation varies locally (see shaded areas in the circled regions in Figs. 4.2 and 4.3). The transition zones showing large variations in saturation indicate higher probabilities to shift to new interfacial configurations in response to small perturbations in capillary pressure or saturation. Quantifying such relations can provide useful information on how and where cavitation occurs, or to identify preferential flow paths in porous materials. The methodology provides a route from grain or pore scale structure to capillary structure and thus macroscopic constitutive relationships that would be otherwise difficult to obtain.

4.7. References Cited

[1] P. G. de Gennes, F. Brochard-Wyart, and D. Quere, *Capillarity and Wetting Phenomena: Drops, Bubbles, Pearls, Waves.* Springer, 2004.

[2] J. N. Israelachvili, *Intermolecular and Surface Forces: Revised Third Edition*. Academic Press, 2011.

[3] R. A. Fisher, “On the capillary forces in an ideal soil; correction of formulae given by W. B. Haines,” *J. Agric. Sci.*, vol. 16, no. 03, p. 492, Mar. 1926.

[4] G. Mason and W. C. Clark, “Liquid bridges between spheres,” *Chem. Eng. Sci.*, vol. 20, no. 10, pp. 859–866, 1965.

[5] F. M. Orr, L. E. Scriven, and A. P. Rivas, “Pendular rings between solids: meniscus properties and capillary force,” *J. Fluid Mech.*, vol. 67, no. 04, p. 723, Mar. 2006.

[6] T. Gröger, U. Tüzün, and D. M. Heyes, “Modelling and measuring of cohesion in wet granular materials,” *Powder Technol.*, vol. 133, no. 1, pp. 203–215, 2003.

[7] P. Pierrat and H. S. Caram, “Tensile strength of wet granula materials,” *Powder Technol.*, vol. 91, no. 2, pp. 83–93, 1997.

[8] V. Richefeu, M. El Youssoufi, and F. Radjaï, “Shear strength properties of wet granular materials,” *Phys. Rev. E*, vol. 73, no. 5, p. 051304, May 2006.

[9] Z. Grof, C. J. Lawrence, and F. Štěpánek, “The strength of liquid bridges in random granular materials,” *J. Colloid Interface Sci.*, vol. 319, no. 1, pp. 182–192, 2008.

[10] J. Lechman and N. Lu, “Capillary Force and Water Retention between Two Uneven-Sized Particles,” *J. Eng. Mech.*, vol. 134, no. 5, pp. 374–384, May 2008.

[11] D. J. Hornbaker, R. Albert, I. Albert, A.-L. Barabasi, and P. Schiffer, “What keeps sandcastles standing?,” vol. 387, no. 6635, p. 765, Jun. 1997.

[12] S. Nowak, A. Samadani, and A. Kudrolli, “Maximum angle of stability of a wet granular pile,” *Nat. Phys.*, vol. 1, no. 1, pp. 50–52, Oct. 2005.

[13] M. Chen, C. Yang, and Z.-Y. Guo, “A Monte Carlo simulation on surface tension of liquid nickel,” *Mater. Sci. Eng. A*, vol. 292, no. 2, pp. 203–206, Nov. 2000.

[14] E. V Albano, K. Binder, and W. Paul, “Capillary condensation in the two-dimensional lattice gas: A Monte Carlo test of fluctuation corrections to the Kelvin equation,” *J. Phys. A. Math. Gen.*, vol. 30, no. 10, pp. 3285–3297, May 1997.

[15] J. Reszko-Zygmunt, O. Pizio, W. Rzysko, S. Sokolowski, and Z. Sokolowska,

"Capillary Condensation in Pores with Energetically Heterogeneous Walls: Density Functional versus Monte Carlo Calculations.," *J. Colloid Interface Sci.*, vol. 241, no. 1, pp. 169–177, Sep. 2001.

[16] D. Cao and W. Wang, "Grand canonical Monte Carlo simulation of methane adsorbed in layered pillared pores," *Phys. Chem. Chem. Phys.*, vol. 3, no. 15, pp. 3150–3155, Jan. 2001.

[17] L. D. Gelb, "The ins and outs of capillary condensation in cylindrical pores," *Mol. Phys.*, vol. 100, no. 13, pp. 2049–2057, Jul. 2002.

[18] B. Coasne and R. J.-M. Pellenq, "A grand canonical Monte Carlo study of capillary condensation in mesoporous media: effect of the pore morphology and topology.," *J. Chem. Phys.*, vol. 121, no. 8, pp. 3767–3774, 2004.

[19] R. Paul and H. Rieger, "Condensation phenomena in nanopores: a Monte Carlo study.," *J. Chem. Phys.*, vol. 123, no. 2, p. 24708, Jul. 2005.

[20] D. H. Rothman and S. Zaleski, "Lattice-gas models of phase separation: interfaces, phase transitions, and multiphase flow," *Rev. Mod. Phys.*, vol. 66, no. 4, pp. 1417–1479, Oct. 1994.

[21] D. P. Landau and K. Binder, *A Guide to Monte Carlo Simulations in Statistical Physics*, vol. 13. Cambridge University Press, 2005.

[22] M. Van Genuchten, "A closed-form equation for predicting the hydraulic conductivity of unsaturated soils," *Soil Sci. Soc. Am. J.*, vol. 44, no. 5, pp. 892–898, 1980.

[23] N. Lu and W. J. Likos, *Unsaturated Soil Mechanics*. Wiley, 2004.

[24] N. Lu, T.-H. Kim, S. Sture, and W. J. Likos, "Tensile Strength of Unsaturated Sand," *J. Eng. Mech.*, vol. 135, no. 12, pp. 1410–1419, Dec. 2009.

CHAPTER 5

Hysteresis of Liquid Adsorption in Porous Media by Coarse-Grained Monte Carlo with Direct Experimental Validation

A paper submitted to the Journal of Chemical Physics

Benjamin D Zeidman[1], Ning Lu[2], and David T. Wu[3]

5.1. Abstract

The effects of path-dependent wetting and drying manifest themselves in many types of physical systems, including nanomaterials, biological systems, and porous media such as soil. It is desirable to better understand how these hysteretic macroscopic properties result from a complex interplay between gasses, liquids, and solids at the pore scale. Coarse-Grained Monte Carlo (CGMC) is an appealing approach to model these phenomena in complex pore spaces, including ones determined experimentally. We present two-dimensional CGMC simulations of wetting and drying in two systems with pore spaces determined by sections from micro X-ray computed tomography: a system of randomly distributed spheres and a system of Ottawa sand. Results for the phase distribution, water uptake, and matric suction when corrected for extending to three dimensions show excellent agreement with experimental measurements on the same systems. This supports the hypothesis that CGMC can generate metastable configurations representative of experimental

[1] Graduate student and primary researcher, Department of Chemistry and Geochemistry, Colorado School of Mines.
[2] Primary author, Department of Civil and Environmental Engineering, Colorado School of Mines.
[3] Department of Chemistry and Geochemistry, Colorado School of Mines.

hysteresis, and can also be used to predict hysteretic constitutive properties of particular experimental systems given pore space images.

5.2. Introduction

Hysteretic behavior related to adsorption of fluids in porous materials exists in myriad natural systems. In nanotechnology, the properties that can be calculated from phase adsorption studies include pore size, shape, distribution, adsorption isotherms, liquid-vapor coexistence curves, and ion channel diffusion [1–3]. In medicine, the study of dental surfaces and bone formation, which can lead to the design of better therapies, hysteretic behavior has been observed [4, 5]. Soil stability is affected by the hysteretic nature of fluid flow through a granular pile [6]. Adsorption at the meso-scale is of particular interest [7], as it can reveal much significant information about granular systems, including pore size distribution, pore shape, permeability, and surface area.

Adsorption of fluids in soils involves a complex interplay of gasses, liquids, and solids [8, 9]. Various experimental and theoretical approaches have been developed to investigate adsorption in porous materials. Experimental methodologies typically measure water retention within porous media using transient flow methods [10, 11]. Theoretical approaches to address multiphase distribution in porous materials include modeling fluid flow via solutions to the Navier-Stokes equations [12, 13], molecular-scale Monte Carlo [14], Monte Carlo annealing methods [15], grand canonical Monte Carlo simulations [3, 16, 17] and density functional theory [18]. In soils specifically, several theoretical models have been proposed for constitutive properties such as soil-water retention [19, 20]. Approaches to determine the phase distribution using continuum methods become more difficult with increasing complexity of the pore space,

while techniques such as molecular dynamics [21] or computational fluid dynamics [22] can have significant computational expense.

When porous materials are exposed to wetting or drying conditions the fluid content and distribution through the material is typically hysteretic in nature. This results in a history dependence for many resulting properties, which in the case of soils includes key constitutive properties such as adsorption isotherms and soil-water retention curves. Thus, it is important for simulation methodologies to be able to capture and quantify hysteresis in fluid retention under wetting and drying conditions. The most prevalent simulation methodology is grand canonical Monte Carlo, using both molecular and lattice models [23]. There is evidence that the hysteretic sampling of configurations by grand canonical Monte Carlo is representative of that using more realistic dynamics [17, 18, 24, 25]. There are several simulation studies on adsorption hysteresis, notably by Monson and coworkers. Many studies consider idealized pore spaces, such as slit or ink-bottle pores [18, 26, 27] or interconnected pore networks [28-30], and focus on the influence of a few parameters, such as pore geometry or temperature. Other studies have looked to examine adsorption/desorption in generated synthetic complex pore spaces, with statistical attributes matched to systems such as porous glass or silica, to illustrate qualitative comparison of the adsorption hysteresis with experimental systems [18, 31-36].

We present here a direct comparison of hysteretic adsorption in coarse-grained Monte Carlo simulation and experimental measurements on the same pore space, allowing for validation of the simulation methodology and derived physical quantities. Experimental input for the simulation include tomographic images of the pore space as

well as contact angle and interfacial free energy values for setting interaction energies between neighboring cells. The simulation methodology uses a two-dimensional (2D) grand canonical extension of our prior study using canonical lattice Monte Carlo, together with geometric corrections to account for using two-dimensional sections of the three-dimensional pore space [24]. Simulation results for the soil-water retention, matric suction and phase distribution, are directly compared with experimental results for the same system.

5.3. Methodology

We consider systems where the temperature is well below the fluid critical point, and with pore sizes large compared to the fluid interfacial width. These are common conditions for many porous systems of interest, including the experimental systems presented here. The confined fluid can thus be considered to consist of continuum liquid and vapor regions separated by well-defined interfaces. For a given thermodynamic condition, there are many such configurations, each corresponding to a metastable local energy minimum. The coarse-grained lattice methodology presented below aims to sample such local minimum energy configurations. To do so, the resolution of the lattice is taken high enough to resolve the smallest pore features of interest, so that the interfacial configurations can approximate that of the continuous real system. Furthermore, the coarse-grained lattice model is simulated at a fictitious temperature that is low enough that the interfaces in the model are also well-defined, but high enough to sample different configurations and avoid low-temperature lattice discretization artifacts. In this way, the configurations in the coarse-grained model can mimic those of the real system by likewise seeking to minimize the interfacial energy.

The parameters of the real system that are needed for the coarse-grained model are thus the interfacial energies, which control the contact angles, and the amount (or chemical potential) of the fluid phase. Because of this, the coarse-grained model captures the interfacial behavior at a particular thermodynamic condition of the real fluid. Behavior at different thermodynamic conditions, reflecting the phase behavior of the fluid, would be captured by changing the interfacial tensions and chemical potentials.

Our simulation methodology is based on a lattice gas adapted for granular systems [15, 37-39] and an extension of our previous work [24]. The model consists of a grand canonical lattice gas with each lattice cell representing a coarse-grained region consisting of one of three phases: gas, liquid, or solid. The effective Hamiltonian can then be defined as

$$E = \sum_{i,j} \sum_{\alpha,\beta} J_{\alpha\beta} n_i^{\alpha} n_j^{\beta} + \mu \sum_i n_i^{\lambda} \quad (5.1)$$

where μ is the chemical potential for a cell in the liquid phase λ, the first sum is over all nearest neighbor cells i and j, and the second sum is over all phases. The occupation number for the cell is thus defined as $n_i^{\alpha} = 1$ if cell i is in phase α and 0 otherwise. The coarse-grained interfacial coupling parameters, $J_{\alpha\beta}$, account for the (free) energy of contact between neighboring cells of phase α and β. We note that the Hamiltonian for a given set of $J_{\alpha\beta}$ with non-zero values of same-phase coupling parameters, $J_{\alpha\alpha}$, can be rewritten as an equivalent Hamiltonian with $J_{\alpha\alpha} = 0$ by replacing the different-phase coupling parameters $J_{\alpha\beta}$ with their relative values $J_{\alpha\beta} - (J_{\alpha\alpha} + J_{\beta\beta})/2$ and with an appropriate shift in the chemical potential values.

While this lattice gas model can be simulated in three dimensions to match the experimental system, for computational efficiency we have chosen to use a two-dimensional square lattice to represent the system. We have previously demonstrated that stereological corrections for extrapolating from two to three dimensions have been quantitatively accurate for characteristic interfacial properties such as the capillary pressure and specific surface area [24, 25]. This stereological correction involves using two-dimensional cross-sectional slices of the full three-dimensional pore space as the two-dimensional pore space simulation geometry. The primary assumption is that the distribution of local orientations of the interface are isotropically homogeneous in the three-dimensional system. The functional form depends on the property being measured; e.g. for the capillary pressure, the average radius of curvature is assumed to be the same in 2D and 3D, and for the specific surface area, a standard stereological factor of (4/π) is used to correct from 2D average perimeter/area to 3D average surface area/volume. This resulted in quantitative agreement within error bars of ~8% compared to experiment over the liquid saturation range of 15-70% [24, 25].

For a fluid-fluid interface, the $J_{\alpha\beta}$, are related to the interfacial free energies, $\gamma_{\alpha\beta}$, via the relation [40]:

$$\gamma_{\alpha\beta} l = 2J_{\alpha\beta} - T \ln\left[\coth\left(J_{\alpha\beta}/T\right)\right], \tag{5.2}$$

where the first term on the right-hand side is the free energy of the direct contact, and the second term reflects the contribution due to interfacial fluctuations. Here T represents a (fictitious) simulation temperature that we discuss further below, and we have chosen units of temperature so that Boltzmann's constant takes the value $k_B = 1$. However, since we are interested in mechanically stable, locally minimum energy

configurations expected at the pore scale, the temperatures simulated are relatively low, i.e., $T < J_{\alpha\beta}$. In this regime, the interfacial fluctuation contribution of Eq. 2 is at most 15% of the first term at the upper end of this temperature range, and less for lower temperatures. For a fluid-solid interface, the interfacial fluctuations will be greatly suppressed since the solid is static, and so the interfacial free energy is expected to be closely approximated by the direct contact value of 2 $J_{\alpha\beta}$.

The interactions between phases in the simulation are thus set according to the interfacial free energies (surface tensions) between the phases. However, we further note that the results of the simulation in the limit of $T << J_{\alpha\beta}$ are not dependent on the individual surface tensions, but rather on the ratio of surface tensions set by the contact angle θ as given by Young's equation [41]:

$$\cos\theta = (\gamma_{\mathrm{SG}} - \gamma_{\mathrm{SL}})/\gamma_{\mathrm{LG}} \tag{5.3}$$

As discussed above, the lattice resolution (250x250 in this work) is chosen high enough so that the resulting thermally averaged interfaces are representative of the limiting continuum interfaces, and the solid surface can be considered locally smooth, except for the very smallest pore dimensions. The use of Young's equation under these conditions was quantitatively validated in modeling of complex experimental pore spaces [24, 25].

Contact angle hysteresis is not seen in simulation, because our simulation does not explicitly model fluid flow. Instead, water and gas are transported by randomly selecting a location on the lattice and attempting to change its occupation to the other phase (e.g. changing a location occupied with water to occupying it with air). The earlier canonical version of the algorithm differs only in that a change of air to water in

one location occurs simultaneously with a change of water to air in a different location, to conserve the total amount of each phase. The simulation methodology has no mechanism to move the water phase separately around the pore space. Thus, the observed contact angle in simulation is independent of wetting or drying conditions and is only determined by the ratios of the surface tensions between the different phases: solid-gas, solid-liquid, and liquid-gas (γ_{SG}, γ_{SL}, and γ_{LG}, respectively). To correspond to perfect wetting conditions favoring water adsorption onto the solid phase, the interfacial coupling parameters, $J_{\alpha\beta}$, used in this paper were set to -1 for liquid/liquid, +1 for liquid/gas interactions, -2 for liquid/solid interactions, and 0 for all other pairs. A perfect wetting contact angle is analogous to a system of water, quartz/silica sand, and air [15].

The simulation is evolved using the standard Metropolis algorithm [42] and aims to fin the local minimum energy configurations, which conceptually corresponds to an energy scale of $T << J_{\alpha\beta}$. However, for such temperatures (corresponding to the realistic situation of thermal energy producing negligible interfacial fluctuations), the simulation would in practice be unable to overcome the energy barriers between configurations, which correspond to local energy minima; thus, the simulation would be very inefficient. In this respect, $k_B T$ essentially controls the degree to which unfavorable energy transitions are accepted. The temperature dependence on adsorption also manifests itself when considering relative pore size. Within a given pore space, smaller versus larger pores may experience different wetting behaviors at different temperatures. In order for the simulation to maintain efficiency, we chose a temperature similar in scale to $J_{\alpha\beta}$ to speed up the sampling of the many local energy configurations present in a

geometrically complex pore space. For the calculations herein, we have used a fictitious value of $T = 1$, as our J values are order unity.

We prepare the initial conditions of our simulations using the following procedure. The simulation domain is initially populated with the solid phase. The geometry of the solid phase is obtained from experimental methods such as microXCT or other imaging techniques (see Fig. 5.1), and the geometry of the image is discretized onto the simulation lattice. The solid phase is assumed to be stationary. For simulations of wetting (drying), the remaining cells are all assigned as gas (water). We define simulation saturation (as a percentage) as the number of water cells divided by the total number of pore space cells. Note that the simulation methodology is the same regardless of the complexity of the pore space geometry or the magnitude of the pore scale l, though physical quantities will scale with l accordingly.

Experimental results were obtained using a sample of Ottawa sand and tested according to a procedure outlined by Lu et al. 2006 [43].

5.4. Hysteresis in randomly distributed spheres

Initial simulations were conducted on a system of randomly distributed spherical beads. The geometry of this system corresponds to an experimental setup in which capillarity was measured using glass beads (400–600 μm diameter) and imaged using microXCT [24, 25]. Figure 5.1a–b illustrate typical snapshots from a canonical Monte Carlo simulation [24, 25] of the phase distribution in this porous medium, comparing experimental images with simulation output simulation at 25% water saturation. There is close but not perfect correspondence between the water-distribution patterns, which

is expected given the existence of multiple similar local minima for the same degree of saturation.

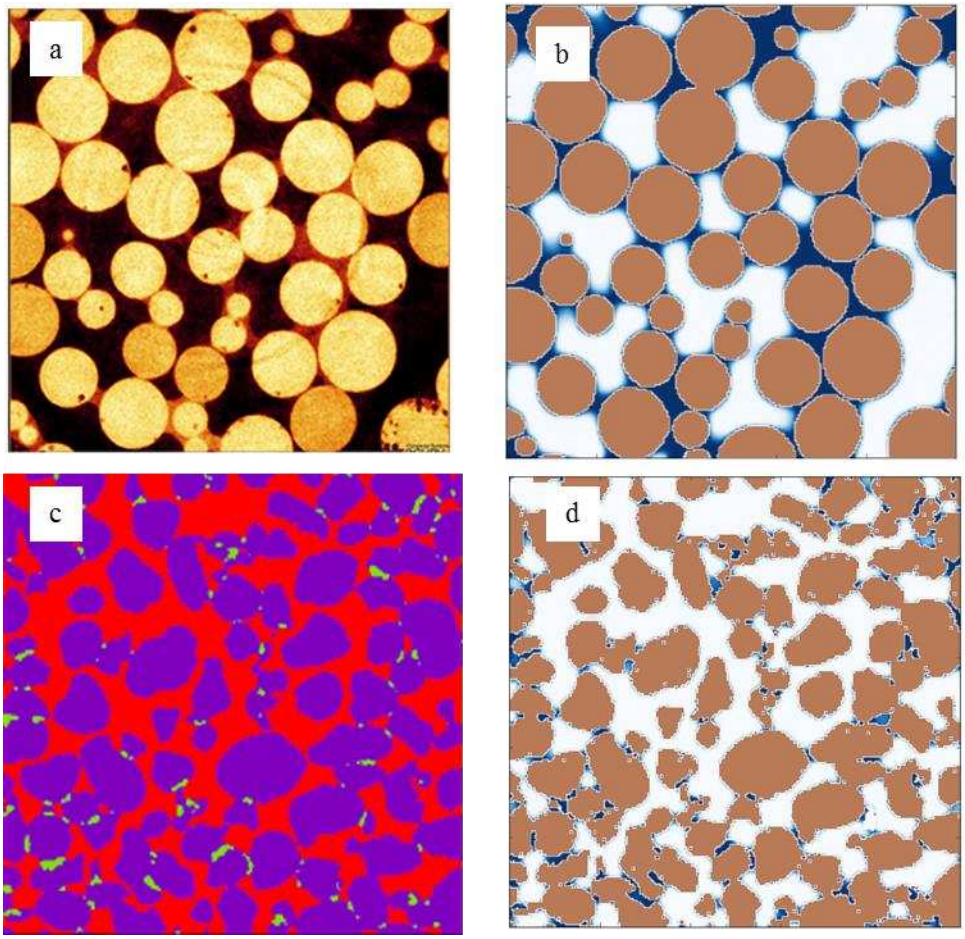

Figure 5.1: A comparison between experimental wetting seen in randomly distributed spheres and microXCT of Ottawa sand and canonical simulation output. (a) a microXCT image of partially saturated glass beads 400–600 μm in diameter. Air, liquid, and beads are shown in black, red, and yellow, respectively. (b) Simulation output at 25% liquid saturation with a similar capillary structure. Air, liquid, and beads are shown in white, blue, and brown, respectively. (c) A microXCT image of partially wet Ottawa sand with dimensions of 3.521 × 3.521 mm and a pixel resolution of 10.06 μm. Air, liquid, and the granular phase are shown in red, green, and purple, respectively. (d) Simulation output at 10% liquid saturation with a similar capillary structure. Air, liquid, and the granular phase are shown in white, blue, and brown, respectively.

To calculate adsorption isotherms, two series of simulations were run with fixed chemical potential values of 2.00–3.00 (units of $k_B T$). Chemical potential plays an analogous role to vapor pressure in experiment in controlling the water saturation. Since

the system is incompressible, the simulation chemical potential is the same as the simulation pressure. The first and second series simulated drying and wetting conditions, in which the initial saturation was set to 100% and 0%, respectively. For each chemical potential value, a discrete simulation was allowed to evolve for 8000 Monte Carlo steps. This allows time for the simulation to equilibrate and observe any substantial wetting (or drying) events. Fig. 5.2 shows the differences in the water distribution between drying (Fig. 5.2a-d) and wetting (Fig. 5.2h-e) for equal values of chemical potential.

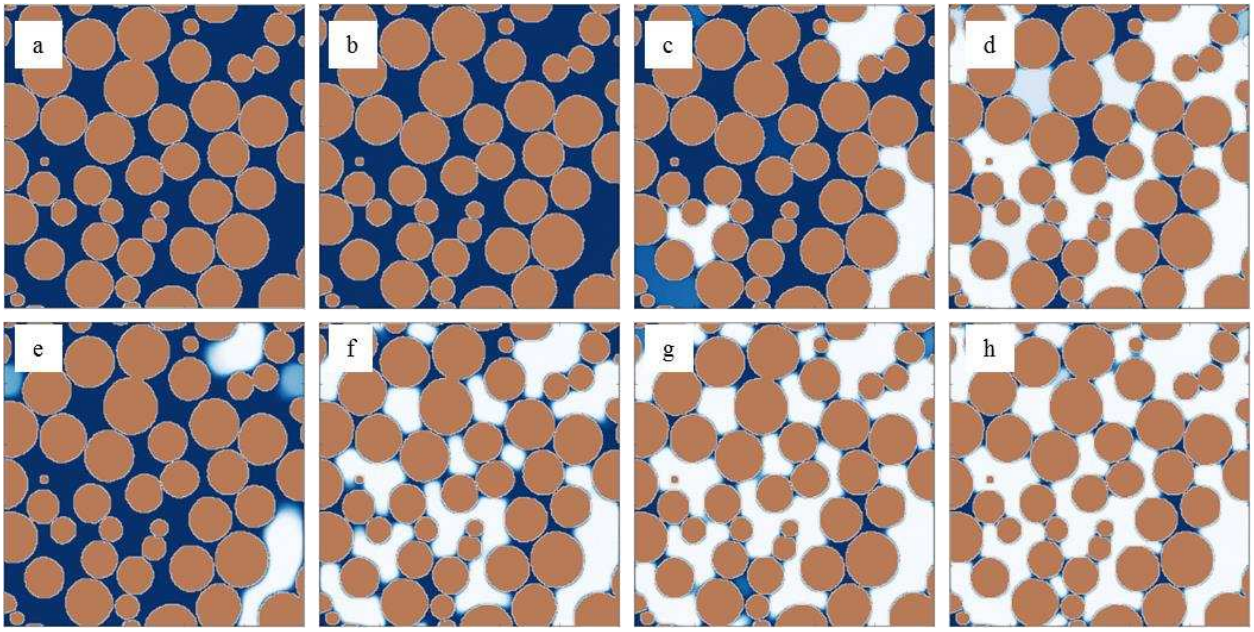

Figure 5.2: Simulation output showing water distributions at chemical potential values of 2.1, 2.25, 2.35, and 2.45. Drying is shown in panels a-d, and wetting in panels h-e. Notice that despite having the same chemical potential values, the resulting capillary distributions are quite different between the wetting and drying cases. Intensity of blue color corresponds to the average water fraction.

Fig. 5.3 shows the adsorption and desorption hysteresis by varying chemical potential for wetting and drying. While both cases show decreasing saturation with increasing chemical potential, the drying simulations maintain more water than the

wetting simulations at a given chemical potential, since they start at full saturation and remove water.

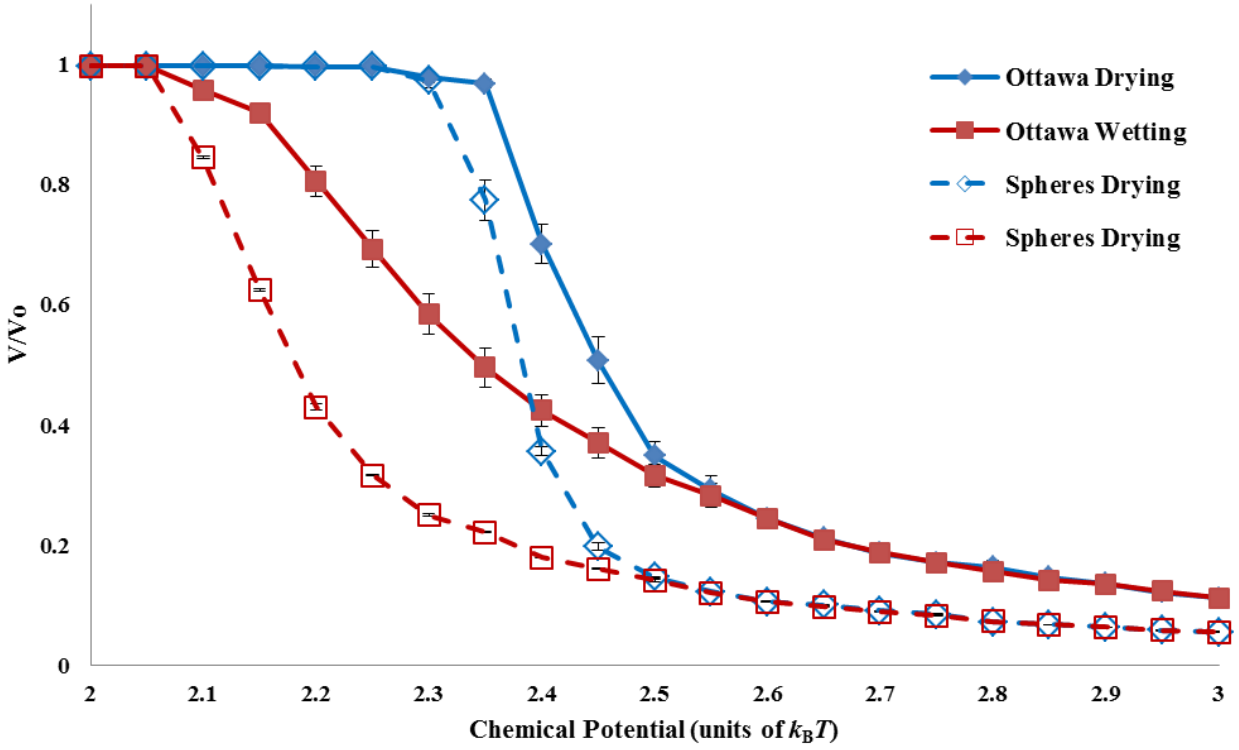

Figure 5.3: Adsorption isotherms for wetting and drying behavior in Ottawa sand (solid line) and randomly distributed spheres (dashed line). Drying and wetting are represented as blue diamonds and red squares respectively. Plotted is the fraction of water cells (since the simulation is a 2D area of water cells it is analogous to volume) vs. chemical potential (units of k_BT). V is the simulation saturation level and V_0 is the 100% saturation level. Each data point corresponds to four discrete simulations at the given chemical potential value; in many cases the associated error bars are less than the size of the plot symbol.

As the chemical potential is increased above its initial value a separation in the isotherms emerges. This begins at a chemical potential value of 2.05. The drying curve stays close to 100% saturation until a chemical potential value of 2.25 is reached; at this point, the difference between the two curves is greatest at 66% saturation. The two isotherms converge again at a chemical potential of 2.5. The simulation panels in Fig.

5.2 all correspond to this region of hysteresis (isotherm separation) from the plot in Fig. 5.3.

5.5. Hysteresis in Ottawa Sand

Grand canonical Monte Carlo simulations were then carried out on a pore space derived from an experimental sample of Ottawa sand. The geometry was determined using 2D cross-sections of a three-dimensional (3D) X-ray computed tomography image. An example 2D cross section along with a representative simulation at a similar saturation is shown in Fig. 5.1c–d. The distribution of the water phase is again similar between experiment and simulation. Calculations were conducted in the same manner as for the systems with randomly distributed spheres.

Because of the increased complexity of this geometry, the manner in which the pore space is populated with liquid is not always consistent between wetting and drying simulations. Fig. 5.4a–d illustrates this by comparing wetting and drying simulations at similar saturation levels but different chemical potential values. A noticeable detail in Fig. 5.4, particularly panels a and b, is the areas of water phase that are lighter in color than other areas of adsorbed water in the pore space. This indicates that either wetting or drying took place in this area during sampling to determine the equilibrium water distribution. Wetting or drying of a specific pore space location occurred when the simulation overcame an energy barrier in a region that was previously at local equilibrium. This is discussed more thoroughly in the next section. When this occurs during a canonical simulation, it appears visually identical to the light blue regions in Fig. 5.4. During a grand canonical simulation, water in this region is either added or removed from the simulation, analogous to cavitation [44]. In canonical simulation the water is

redistributed elsewhere in the pore space. The corresponding adsorption isotherms for the Ottawa sand are given in Fig. 5.3 with a similar trend as seen with the adsorption isotherms for the randomly distributed spheres.

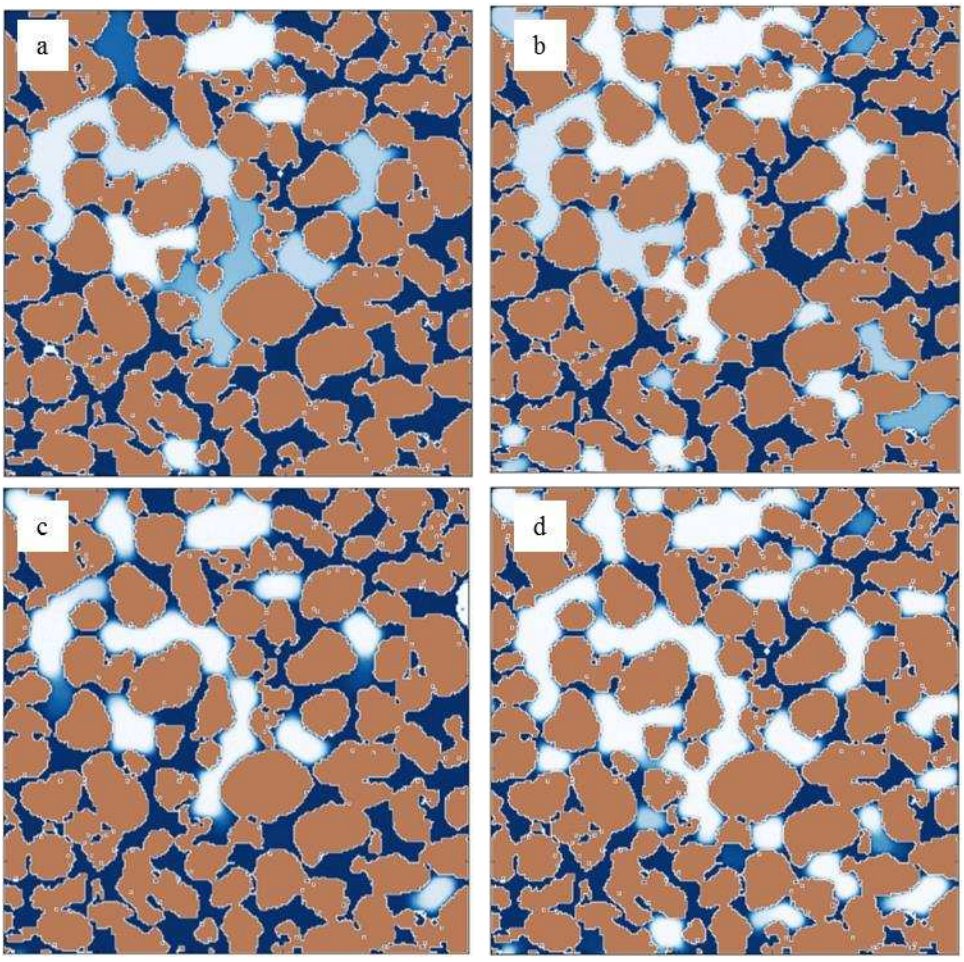

Figure 5.4: Capillary structure of samples with similar water saturation but different chemical potentials depending on whether wetting and drying. (a) is a wetting condition with a chemical potential value of 2.45, and (c) is a drying condition with a chemical potential value of 2.25, yet both (a) and (c) yield similar saturation conditions of about 70%. Similarly, panels (b) and (d), with chemical potential values of 2.4 and 2.35, respectively, yield similar saturation values of about 50%. Intensity of blue color corresponds to the average water fraction.

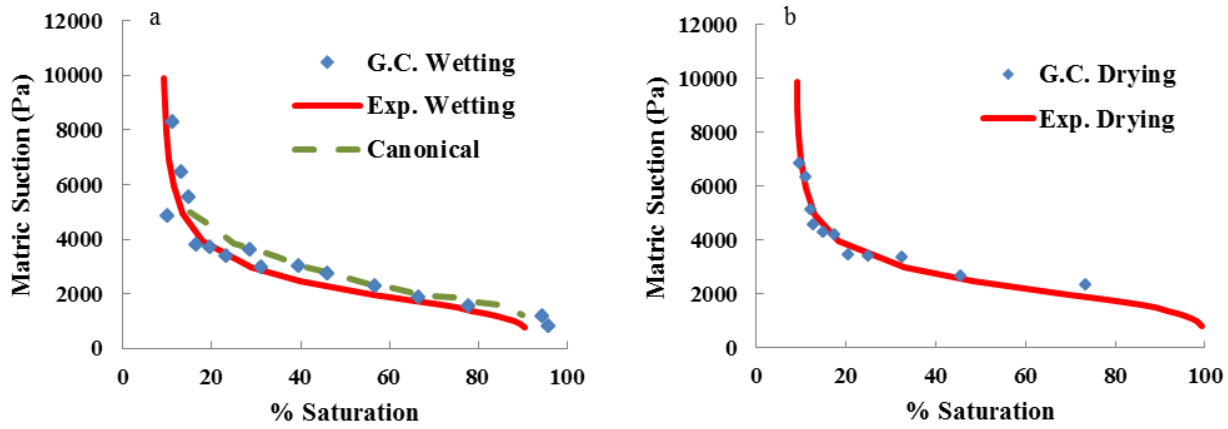

Figure 5.5: Calculated soil-water retention curves (SWRC) for the Ottawa sand system (matric suction [kPa] vs. percent saturation). The simulation results are averages of the principal radii of curvature between the water and air phases converted to matric suction with the Laplace-Young equation. (a) SWRC under drying conditions, and (b) SWRC under wetting conditions. Grand canonical simulation, canonical simulation, and experimental results are shown in blue, green, and red respectively. Canonical simulation results are included with the wetting SWRC because canonical simulation begins with the water phase randomly distributed in the pore space and then adsorbing onto the material as the simulation progresses. Experimental results were obtained using a sample of Ottawa sand and tested according to a procedure outlined by Lu et al. 2006 [43].

From these data, it is possible to calculate the soil-water retention curve (SWRC), which relates the soil suction to the volumetric water content and is a key piece of information used to understand the hydrologic cycle [45]. Matric suction is the pressure difference between the air and water phases and can be calculated using the Laplace-Young equation: $\Delta P = 2\gamma_{LG} / r$, where r is the average radius of curvature of the local liquid-gas interfaces. From the simulation data, we define the air-liquid interface as a 50% contour of the average liquid saturation, and determine the local radius of curvature from a least squares fit [24]. The factor of two in the Laplace-Young equation reflects the existence of two principal radii of curvature (e.g., r_1 and r_2) [9, 24]. We have assumed that the average curvature in the two dimensional simulations can be used as the average in three dimensions. Given the image scale, the value for the cell length (l)

is 13.284 μm. The literature value for the surface tension of water at 25℃ (γ_{LG}; 71.79 dyn/cm) was used.

Figure 5.5 plots the SWRC given by grand canonical simulation, canonical simulation, and experiment. The results for the canonical simulation are included with the wetting data, because the process captured by canonical simulation is more similar to grand canonical wetting. Under canonical conditions, the water phase starts as a randomly distributed “vapor” in the pore space and then condenses on the surface of the solid. In contrast, in the drying condition, the simulation starts as fully saturated, as seen in Fig. 5.5b. In both cases, the simulation data agree with the experimental data. This is significant, because it provides a concrete link between simulation output and the constitutive, macroscopic properties of soils.

A potential source for the differences between the grand canonical simulation and experiment is the use of approximate dynamics in the evolution of the simulated phase distribution. Under experimental conditions, there is the flow of water during drying and wetting, which can result in contact angle hysteresis [46]. As mentioned earlier, the effects of contact angle hysteresis are not captured by the simulation, and so the observed contact angles will be the same under both wetting and drying conditions. In the simulations, exchange between the water and air phases is allowed at any random location in the pore space, in contrast to experimental conditions, in which fluid must physically flow through the pore structure in order to fill the pore space. In any experiment, trapped pockets of air due to water in the capillaries would almost certainly exist; these are not taken into account in our simulation. However, the good agreement between our simulation and experimental drying and wetting data in Fig. 5 suggests that

despite the physical differences in the microscopic mechanism of mass transport, much of the hysteretic behavior can be captured within this methodology.

5.6. Discussion

As seen in Fig. 5.3, the hysteresis loops in the adsorption isotherms of the glass beads and Ottawa sand differ substantially in location and shape, reflecting differences in the respective distribution, geometry and size between the pore spaces of the two samples. The pore space in the glass bead and Ottawa sand simulations occupy 40% and 35% of the total simulated area, respectively. Hysteresis reflects how the energy required to add or remove water from a lattice cell depends on that cell's surroundings. In the case of wetting a dry system, adding water to a single cell in a dry area is unfavorable energetically. Moreover, it is more energetically intensive to populate (or unpopulate) larger pore spaces. Likewise, removing water from a cell in an already established water region is also energetically unfavorable. This causes the branching between the wetting and drying paths that is seen in the adsorption isotherms. The ability for the methodology to capture the character of the hysteresis from experimental images in the isothermal adsorption curves is an advantage when compared to extrapolations from simpler geometries [3, 18].

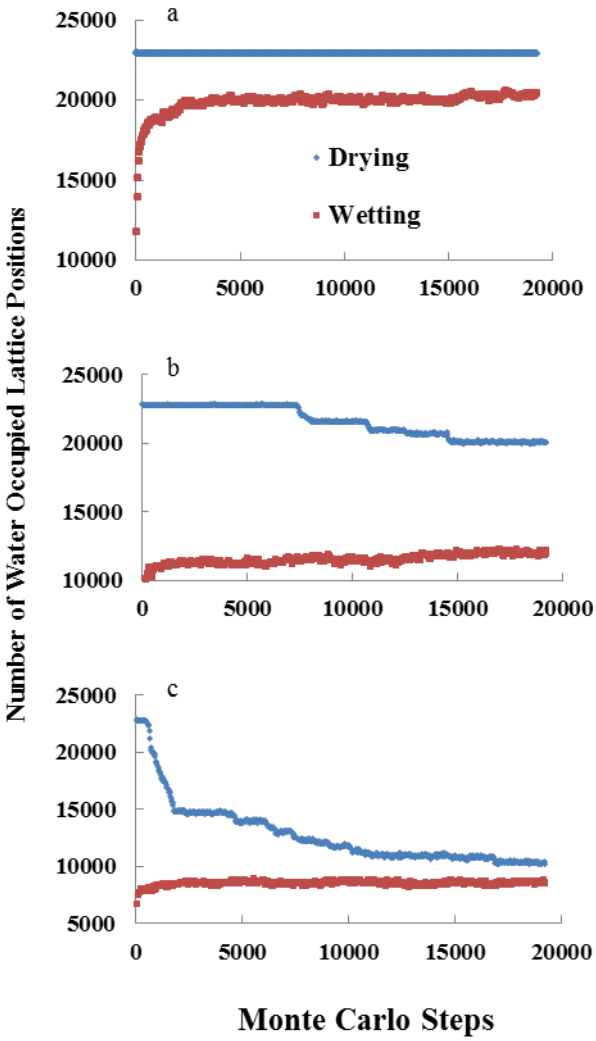

Figure 5.6: A representation of simulation equilibration by comparing the number of liquid cells to Monte Carlo steps. (a), (b), and (c) depict simulations at chemical potentials of 2.20, 2.35, and 2.45 (units of kBT), respectively. In all figures, the top (blue) curve represents drying conditions, and the bottom red curve represents wetting conditions. In all cases, as the simulation progresses, the two curves trend towards each other, to a presumed equilibrium at extremely long times exceeding practical limitations.

The wetting or drying system moves towards lower free energy through an energy landscape of multiple local minima. This gradually slowing relaxation through metastable states is seen in the plots in Fig. 5.6 of the amount of liquid vs. simulation cycles for both the drying and wetting cases. Hypothetically, given a long enough

timescale, equilibration would result in the same state under the wetting and drying conditions, whether for simulation or experiment, eliminating the hysteresis. As mentioned above, the evolution of the phase distribution by Grand Canonical Monte Carlo is approximate, notably in neglecting fluid dynamics. That the behavior of the properties predicted from simulation compare well with experiments suggest that the evolution by Grand Canonical Monte Carlo captures relevant aspects of the real dynamical evolution of the system. In effect, these results suggest that the wetting and drying hysteresis is largely determined by the pore space geometry without explicit consideration of capillary evolution due to flow. One possible explanation is that the evolution of the phase distribution is quasistatic, controlled by capillary stresses over viscous or inertial stresses. Indeed, for many mesoscale systems, the pore-scale capillary number, $Ca = \mu v/\gamma$, (where μ is the viscosity, v is the pore-scale velocity, and γ is the fluid/fluid interfacial tension) is small (e.g., $Ca \sim 10^{-6}$ - 10^{-4} for oil trapped in pores of water-wet rock [47].

Since the method employs a coarse-grained lattice approach to a complex geometry, simulation is possible on the scale of one's choice for the system. Geometry from various experimental sources (e.g., microXCT or electron microscopy) can be discretized onto a lattice. Associated interfacial properties of different-sized systems are determined by the lattice cell length scale. For example, if the 3.521 × 3.521 mm cell of the Ottawa sand (Fig. 5.4) were 1/100 of that size, the corresponding calculated soil-water retention curves (Fig. 5.5) would retain the same shape, but the capillary pressure would be multiplied by a factor of 100. Additionally this method can be adapted easily to include additional phases or dimensions.

5.7. Conclusion

We have extended our previous Monte Carlo methodology to study path-dependent adsorption phenomenain granular based amterials and soils. This methodology can be used to ascertain and quantify many of the intrinsic properties associated with path-dependent wetting and drying adsorption in geometrically complex porous media. This model can visually demonstrate where within pore space locations capillarity is likely to occur and the resulting water distributions given a wetting or drying scenario. Analysis of the resulting water distribution can produce isothermal adsorption curves demonstrating how the adsorbed water content of a pore space changes according to wetting vs. drying conditions for a given chemical potential. This is analogous to the plots of pressure vs. liquid content found in experimental adsorption studies. Other important intrinsic physical properties can also be ascertained through simulation: in the case of Ottawa sand, the simulation's calculations of soil water retention are straightforward and conform with experimental observations.

We note one final observation related to the excellent agreement between simulation and experiment. Since the simulation does not capture any effects related to flow, our results suggest that key properties resulting from adsorption phenomena may be largely controlled by the geometry of the pore space, rather than the flow of fluid through it. Fluid flow is determined by the effects of material wettability, contact angle hysteresis, and trapped air, as local capillary formation can bar additional wetting in a given region. This effect may be limited to the types of mesoporous media studied here, as both the randomly distributed spheres and Ottawa soil can be saturated fully. Further study would be required to confirm these observations.

5.8. References

[1] G. M. Torrie, G. Lakatos, and G. N. Patey, “Structure and adsorption of water in nonuniform cylindrical nanopores.,” *J. Chem. Phys.*, vol. 133, no. 22, p. 224703, Dec. 2010.

[2] A. Striolo, “Water self-diffusion through narrow oxygenated carbon nanotubes,” *Nanotechnology*, vol. 18, no. 47, p. 475704, Nov. 2007.

[3] R. Paul and H. Rieger, “Condensation phenomena in nanopores: a Monte Carlo study.,” *J. Chem. Phys.*, vol. 123, no. 2, p. 24708, Jul. 2005.

[4] S. J. Pogorzelski, Z. Berezowski, P. Rochowski, and J. Szurkowski, “A novel methodology based on contact angle hysteresis approach for surface changes monitoring in model PMMA-Corega Tabs system,” *Appl. Surf. Sci.*, vol. 258, no. 8, pp. 3652–3658, Feb. 2012.

[5] M. Urist and L. Peltier, “Bone: formation by autoinduction,” *Clin. Orthop. Relat. Res.*, 2002.

[6] S. Nowak, A. Samadani, and A. Kudrolli, “Maximum angle of stability of a wet granular pile,” *Nat. Phys.*, vol. 1, no. 1, pp. 50–52, Oct. 2005.

[7] G. a Tompsett, L. Krogh, D. W. Griffin, and W. C. Conner, “Hysteresis and scanning behavior of mesoporous molecular sieves.,” *Langmuir*, vol. 21, no. 18, pp. 8214–25, Aug. 2005.

[8] P.G. de Gennes, F. Brochard-Wyart, and D. Quere, *Capillarity and Wetting Phenomena: Drops, Bubbles, Pearls, Waves (Google eBook)*. Springer, 2004.

[9] N. Lu and W. J. Likos, *Unsaturated Soil Mechanics*. Wiley, 2004.

[10] S. L. Houston, W. N. Houston, and A.-M. Wagner, “Laboratory filter paper suction measurements,” *ASTM Geotech. Test. J.*, vol. 17, no. 2, pp. 185–194, 2014.

[11] L. D. Suits, T. C. Sheahan, A. Wayllace, and N. Lu, “A Transient Water Release and Imbibitions Method for Rapidly Measuring Wetting and Drying Soil Water Retention and Hydraulic Conductivity Functions,” *Geotech. Test. J.*, vol. 35, no. 1, p. 103596, 2012.

[12] D. Bresch and B. Desjardins, “On the existence of global weak solutions to the Navier–Stokes equations for viscous compressible and heat conducting fluids,” *J. Math. Pures Appl.*, vol. 87, no. 1, pp. 57–90, Jan. 2007.

[13] V. Garzó, C. Hrenya, and J. Dufty, “Enskog theory for polydisperse granular mixtures. II. Sonine polynomial approximation,” *Phys. Rev. E*, vol. 76, no. 3, p.

031304, Sep. 2007.

[14] R. Ziff, E. Gulari, and Y. Barshad, “Kinetic Phase Transitions in an Irreversible Surface-Reaction Model,” *Phys. Rev. Lett.*, vol. 56, no. 24, pp. 2553–2556, Jun. 1986.

[15] R. Knight, A. Chapman, and M. Knoll, “Numerical modeling of microscopic fluid distribution in porous media,” no. September 1989, pp. 994–1001, 1990.

[16] B. Coasne and R. J.-M. Pellenq, “A grand canonical Monte Carlo study of capillary condensation in mesoporous media: effect of the pore morphology and topology.,” *J. Chem. Phys.*, vol. 121, no. 8, pp. 3767–74, Aug. 2004.

[17] L. Sarkisov and P. A. Monson, “Hysteresis in Monte Carlo and Molecular Dynamics Simulations of Adsorption in Porous Materials,” no. 19, pp. 9857–9860, 2000.

[18] P. A. Monson, “Understanding adsorption/desorption hysteresis for fluids in mesoporous materials using simple molecular models and classical density functional theory,” *Microporous Mesoporous Mater.*, vol. 160, pp. 47–66, Sep. 2012.

[19] A. N. Zhou, “A contact angle-dependent hysteresis model for soil–water retention behaviour,” *Comput. Geotech.*, vol. 49, pp. 36–42, Apr. 2013.

[20] D. M. Pedroso and D. J. Williams, “A novel approach for modelling soil–water characteristic curves with hysteresis,” *Comput. Geotech.*, vol. 37, no. 3, pp. 374–380, Apr. 2010.

[21] H. J. Woo, F. Porcheron, and P. a Monson, “Modeling desorption of fluids from disordered mesoporous materials.,” *Langmuir*, vol. 20, no. 11, pp. 4743–7, May 2004.

[22] D. L. Lakeland, A. Rechenmacher, and R. Ghanem, “Towards a complete model of soil liquefaction: the importance of fluid flow and grain motion,” *Proc. R. Soc. A Math. Phys. Eng. Sci.*, vol. 470, no. 2165, pp. 20130453–20130453, Feb. 2014.

[23] L. D. Gelb and K. E. Gubbins, *Characterisation of Porous Solids V*, vol. 128. Elsevier, 2000.

[24] N. Lu, B. D. Zeidman, M. T. Lusk, C. S. Willson, and D. T. Wu, “A Monte Carlo paradigm for capillarity in porous media,” *Geophys. Res. Lett.*, vol. 37, no. 23, Dec. 2010.

[25] B.D. Zeidman, N. Lu, and D. Wu, "Coarse-Grained Monte Carlo Simulation of the Distribution and Capillarity of Multiple Fluids in Porous Media" in *Pore Scale Phenomena: Frontiers in Energy and Environment*, edited by J. Poate, T.

Illangasekare, H. Kazemi, and R. Kee (World Scientific, Singapore, 2015), pp. 263-278.

[26] A. Winkler, D. Wilms, P. Virnau, and K. Binder, “Capillary condensation in cylindrical pores: Monte Carlo study of the interplay of surface and finite size effects.,” *J. Chem. Phys.*, vol. 133, no. 16, p. 164702, Oct. 2010.

[27] P. T. M. Nguyen, C. Fan, D. D. Do, and D. Nicholson, “On the Cavitation-Like Pore Blocking in Ink-Bottle Pore: Evolution of Hysteresis Loop with Neck Size,” *J. Phys. Chem. C*, vol. 117, no. 10, pp. 5475–5484, Mar. 2013.

[28] J. R. Edison and P. a. Monson, “Dynamic mean field theory of condensation and evaporation in model pore networks with variations in pore size,” *Microporous Mesoporous Mater.*, vol. 154, pp. 7–15, May 2012.

[29] P. Yin and G.-F. Zhao, “Numerical study of two-phase fluid distributions in fractured porous media,” *Int. J. Numer. Anal. Methods Geomech.*, vol. 39, no. 11, pp. 1188–1211, Aug. 2015.

[30] G. Y. Gor, C. J. Rasmussen, and A. V. Neimark, “Capillary condensation hysteresis in overlapping spherical pores: A Monte Carlo simulation study,” *Langmuir*, vol. 28, no. 33, pp. 12100–12107, 2012.

[31] E. Kierlik, P. Monson, M. Rosinberg, L. Sarkisov, and G. Tarjus, “Capillary Condensation in Disordered Porous Materials: Hysteresis versus Equilibrium Behavior,” *Phys. Rev. Lett.*, vol. 87, no. 5, p. 055701, Jul. 2001.

[32] Y. K. Tovbin, D. V. Yeremich, and L. K. Zhidkova, “Vapour–liquid coexisting curves and hysteresis of simple adsorbate in complex porous systems,” *Appl. Surf. Sci.*, vol. 252, no. 3, pp. 591–601, Oct. 2005.

[33] K. Page and P. Monson, “Phase equilibrium in a molecular model of a fluid confined in a disordered porous material.,” *Phys. Rev. E. Stat. Phys. Plasmas. Fluids. Relat. Interdiscip. Topics*, vol. 54, no. 1, pp. R29–R32, Jul. 1996.

[34] P. A. Monson, “Contact angles, pore condensation, and hysteresis: insights from a simple molecular model.,” *Langmuir*, vol. 24, no. 21, pp. 12295–302, Nov. 2008.

[35] R. Cimino, K. A. Cychosz, M. Thommes, and A. V. Neimark, “Experimental and theoretical studies of scanning adsorption–desorption isotherms,” *Colloids Surfaces A Physicochem. Eng. Asp.*, vol. 437, pp. 76–89, Nov. 2013.

[36] D. W. Siderius and L. D. Gelb, “Predicting gas adsorption in complex microporous and mesoporous materials using a new density functional theory of finely discretized lattice fluids.,” *Langmuir*, vol. 25, no. 3, pp. 1296–9, Feb. 2009.

[37] D. L. Silverstein and T. Fort, “Prediction of Water Configuration in Wet Unsaturated Porous Media,” *Langmuir*, vol. 16, no. 2, pp. 839–844, Jan. 2000.

[38] D. L. Silverstein and T. Fort, “Incorporating Low Hydraulic Conductivity in a Numerical Model for Predicting Air−Water Interfacial Area in Wet Unsaturated Particulate Porous Media,” *Langmuir*, vol. 16, no. 2, pp. 835–838, Jan. 2000.

[39] D. L. Silverstein and T. Fort, “Prediction of Air−Water Interfacial Area in Wet Unsaturated Porous Media,” *Langmuir*, vol. 16, no. 2, pp. 829–834, Jan. 2000.

[40] L. Onsager, “Crystal Statistics. I. A Two-Dimensional Model with an Order-Disorder Transition,” *Phys. Rev.*, vol. 65, no. 3–4, pp. 117–149, Feb. 1944.

[41] T. Young, “An Essay on the Cohesion of Fluids,” *Philos. Trans. R. Soc. London*, vol. 95, no. 0, pp. 65–87, Jan. 1805.

[42] N. Metropolis, A. W. Rosenbluth, M. N. Rosenbluth, A. H. Teller, and E. Teller, “Equation of State Calculations by Fast Computing Machines,” *J. Chem. Phys.*, vol. 21, no. 6, p. 1087, 1953.

[43] L. David Suits, T. Sheahan, N. Lu, A. Wayllace, J. Carrera, and W. Likos, “Constant Flow Method for Concurrently Measuring Soil-Water Characteristic Curve and Hydraulic Conductivity Function,” *Geotech. Test. J.*, vol. 29, no. 3, p. 12637, Jan. 2006.

[44] Y. Chen, C. Lu, and L. Wu, “Modelling and computation of unsteady turbulent cavitation flows,” *J. Hydrodyn. Ser. B*, vol. 18, no. 5, pp. 559–566, Oct. 2006.

[45] M. Van Genuchten, “A closed-form equation for predicting the hydraulic conductivity of unsaturated soils,” *Soil Sci. Soc. Am. J.*, vol. 44, no. 5, pp. 892–898, 1980.

[46] R. D. Hazlett and R. N. Vaidya, “Lattice Boltzmann simulations and contact angle hysteresis in convergent–divergent media,” *J. Pet. Sci. Eng.*, vol. 33, no. 1–3, pp. 161–171, Apr. 2002.

[47] A. Cense and S. Berg, “The viscous-capillary paradox in 2-phase flow in porous media,” *Int. Symp. Soc. …*, 2009.

CHAPTER 6

Simulation of Multiple Fluids in a Porous Medium

In this Chapter, I investigate how systems with components different than water, air, and solid behave. Motivated by the complex problem of recovering energy from the environment, two systems were chosen for study. The first system consists of a wetting fluid and a non-wetting fluid meant to simulate clathrate hydrate and water within a pore space. The second system investigated two wetting fluids in competition for adsorption to represent oil and water confined to a pore space. The simulation methodology is identical to the canonical simulation methods discussed in previous chapters, but with interfacial coupling parameters and contact angles appropriate for the representative systems.

6.1. Wetting and Non-wetting Fluids.

This system is analogous to hydrate formation and agglomeration in sediments and is based on the equilibrium between a wetting fluid (water) and a non-wetting fluid (ice) within the pore space. The interfacial free energy values were assigned as 350 mJ/m^2 for quartz-water [1], 532 mJ/m^2 for quartz-ice [2], and 2 mJ/m^2 for the water-ice interaction [3]. In terms of actual simulation coupling parameters, the values were reduced to 175, 266, and 1 respectively with units of k_BT. These values were chosen for several reasons. First, we wanted to use values that correspond to actual experimental conditions, so values the values correspond to quartz for solid, water for the wetting fluid, and ice for the non-wetting fluid. While interfacial free energy values are indeed sensitive to temperature, the actual equilibrium distribution of the phases in the pore

space will be based on the contact angle. It the goal of this investigation is to tie these simulations as closely to experimental conditions as possible, but a diverse collection of experimentally validated interfacial energy parameters for the phases in this system were difficult to obtain. The system at equilibrium should be representative of hydrate formation at geological timescales [4].

Effectively, the system behaves as a fully saturated liquid system with the hydrates phase “floating” around in it. Energetically, the wetting fluid prefers to fully adsorb to the solid phase and is distributed throughout the pore space. Because of the surface tension between the non-wetting fluid and the wetting fluid, non-wetting fluid lattice locations are more energetically stable while located next to other non-wetting fluid cells. Thus the energetically preferred equilibrium is for all of the non-wetting fluid phase to agglomerate and remain as a large spherical conglomerate with in the pore space. How the conglomerate of non-wetting fluid behaves in the pore space depends on two factors, the ratio of the surface free energy to the temperature, and the geometry of the pore space. Since we hold the simulation temperature constant, this leaves only the exploration of the effect pore space geometry has on the distribution of the non-wetting fluid within the pore space. When the amount of non-wetting fluid is less than the volume of individual pores within the pore space, the non-wetting fluid is free to “float about” through the wetting fluid phase within the pore space. It is when the non-wetting fluid volumes start to approach or exceed that of the individual pores, several interesting phenomena are observed.

To begin analyzing how non-wetting fluids and wetting fluids interact within pore space a very simple pore space system was chosen initially. This system consists of

two square shaped pores of differing sizes: a large pore with dimensions 30x30 lattice units and a small pore with dimensions of 20x20 lattice units. This allows simulation results to show where the non-wetting fluid begins agglomerating within the pore space. Figure 6.1 shows the equilibrium distribution for this system in the simple pore space. At low saturations of non-wetting fluid (10%), as shown in Fig. 6.1a, no agglomeration can be seen in the results. The reason no non-wetting fluid is present is that the agglomeration of non-wetting fluid is smaller than the size of both pores. This means that the non-wetting fluid agglomeration is not confined by the pore walls and is freely floating through the open pore space. As the volume of non-wetting fluid is increased, the agglomeration blob now becomes big enough to be confined and is visible in the simulation equilibrium distribution results. As the agglomeration of non-wetting fluid grows in size, it is free to float within the pore space until it becomes smaller than the largest pore, but larger than all other pores. This causes the first visual agglomeration of non-wetting fluid in the simulation results to always appear in the largest pore. This occurred in Fig. 6.1b at a volume of 20% non-wetting fluid. As the agglomeration of non-wetting fluid continues to grow in the larger pore, it begins to encounter the pore walls. Since the interface between the wetting fluid and the non-wetting fluid is soft, the non-wetting fluid blob begins to deform from a sphere and take on a shape closely resembling the pore geometry, as seen in Fig. 6.1c at 50% hydrate saturation level. As even more volume is added the non-wetting fluid agglomeration deforms to a point where it becomes more energetically favorable to break into two separate blobs in both the large and the small pore. This is shown in Fig. 6.1d and occurs at a 52% hydrate saturation level. Numerically this can be seen in Fig. 6.2. This plot shows the fraction of

hydrate located in each pore. Initially, below 20% hydrate saturation, the agglomeration freely floats within the pore space. From 20% to 43% the hydrate agglomeration is confined to the larger pore. Above 43% the transition happens between deformation of the hydrate to match the pore space geometry and breaking off to form a new agglomeration in the small pore.

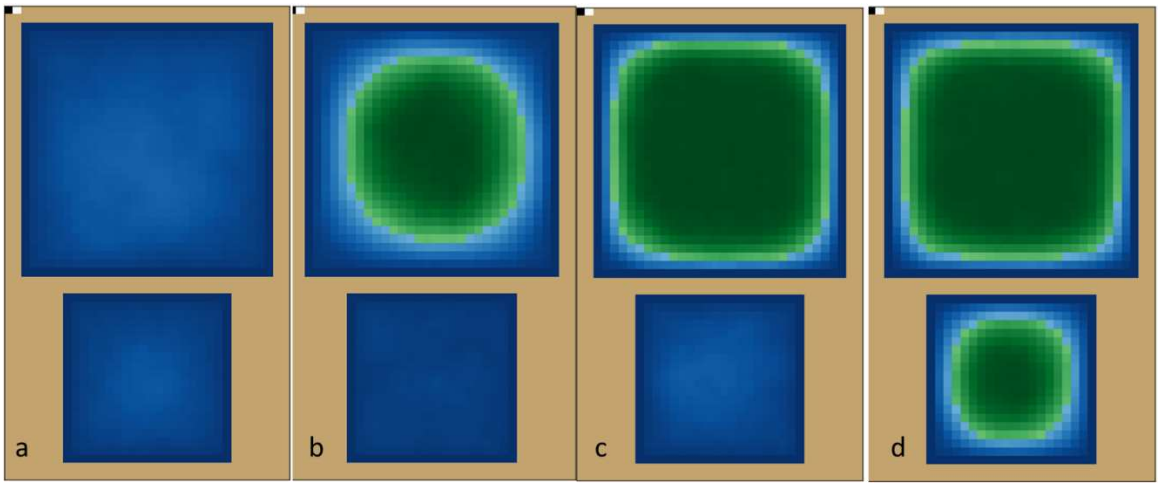

Figure 6.1: Simulation results for water (blue) and hydrate (green) confined to two simple pores. The larger top pore has dimensions of 30x30 lattice units. The smaller bottom pore has dimensions of 20x20 lattice units. a) has a 10% hydrates saturation level, b) 20% hydrate saturation level, c) 50% hydrate saturation level, and d) 52% hydrate saturation level.

Since this simulation methodology is capable of handling very complex geometry, this system has been extended to simulation in a pore space based on Ottawa sand. The results are shown in Fig 6.3. Since the pore space in sediments is inherently random and complex, naturally the system will have locations within the pore space of varied size and shape. Since it follows that the non-wetting fluid will agglomerate in a trend similar to that seen in the simple pore system, at low concentrations no agglomerations are visible in the simulation output. As concentration of non-wetting fluid increases we expect to see spherical agglomeration begin starting

at the largest pore. To make the prediction of where this will happen a heatmap of the pore space is shown in Fig 6.3a. This pore space mapping represents the maximum radius of a sphere inscribed within the pore space centered at the given location. The size distribution in Fig. 6.3a ranges from dark red with a maximum sphere radius of fourteen lattice units to dark blue with a minimum radius of one lattice unit. Fig. 6.3b-c shows simulation results for a varied amount of non-wetting fluid for non-wetting fluid volumes of 5%, 10%, and 15% respectively. At the lowest concentration of non-wetting fluid presented, the first agglomeration point corresponds to the largest are within the pore space (Fig. 6.3b). As the amount of non-wetting fluid increases, the agglomerations of non-wetting fluid distort in shape and form new conglomerates within the pore space. This occurs starting with the largest pore and filling subsequent pores down to smaller ones (Fig. 6.3c and d).

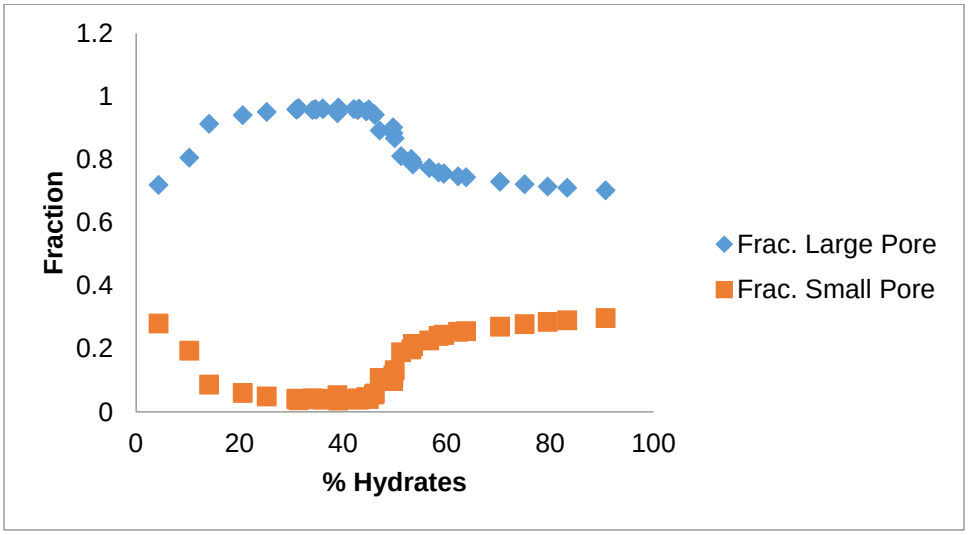

Figure 6.2: Numerical plot showing the distribution of hydrate phase in the simple two pore system.

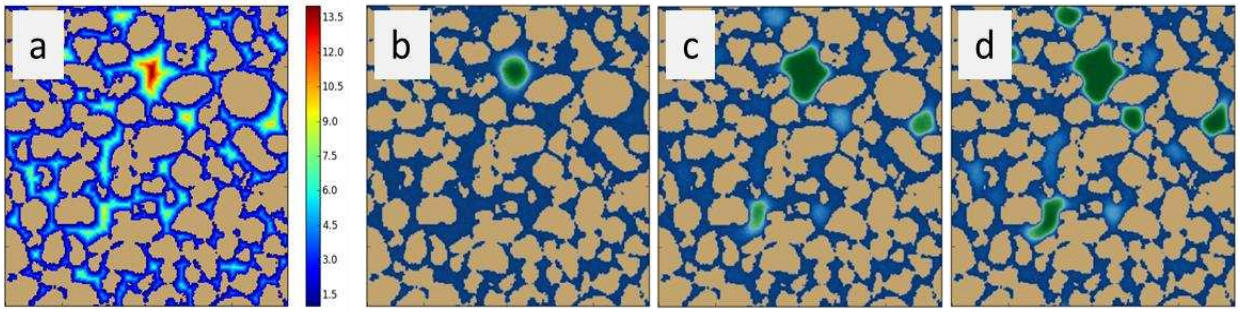

Figure 6.3: Simulation results for hydrate (green) and water (blue) confined to an Ottawa sand pore space. a) Is a heatmap plot of the maximum radius a sphere could have if located at that lattice point. The range is form 0 to 14 as indicated in the colorbar to the right. Panels b-c show simulation results for 5%, 10%, and 15% hydrate saturation levels respectively.

As we have already shown it is possibly to exactly calculate the distribution of non-wetting fluid within a simple pore space. With the observations contained herein it should be possible to develop a methodology able to predict the distribution of non-wetting fluid in a complex pore space without independent Monte Carlo simulation. As the wetting fluid / non-wetting fluid system was chosen specifically to model water and hydrates/ice, this holds excellent promise for applications to the development of technology for harvesting methane reserve currently distributed in the environment as gas hydrates.

6.2. Two Wetting Fluids

We shall now consider a systems consisting of two wetting fluids meant to emulate water and oil. The phases are represented by quartz for the solid, heptane for the oil phase, and water. These systems will be investigated at two different contact angles: 105° and 70°. Interfacial free energy parameters were assigned as follo ws (all values have units of k_BT): For the 105° contact angle system solid-water is 17.7, solid-heptane is 17, and water-heptane is 2.6 [5]. For the 70° contact angle system solid

water is 1, solid-heptane 2.23, and water-heptane is 4 [6]. The real world analogy to these systems is the 105° contact angle system corresponds to pure water, heptane, and quartz. The 70° system consists of pure quartz and heptane, but the water ph ase being doped with a 7.5% NaOH solution. Comparing the two systems allows for investigation of how difference in contact angle affect the wettability between the two fluids. In the case of the pure water system, the oil is more wettable than the water. In the 7.5% NaOH solution system, the water is more wettable than the oil. Fig. 6.4 shows the simulation results for the equilibrium phase distribution.

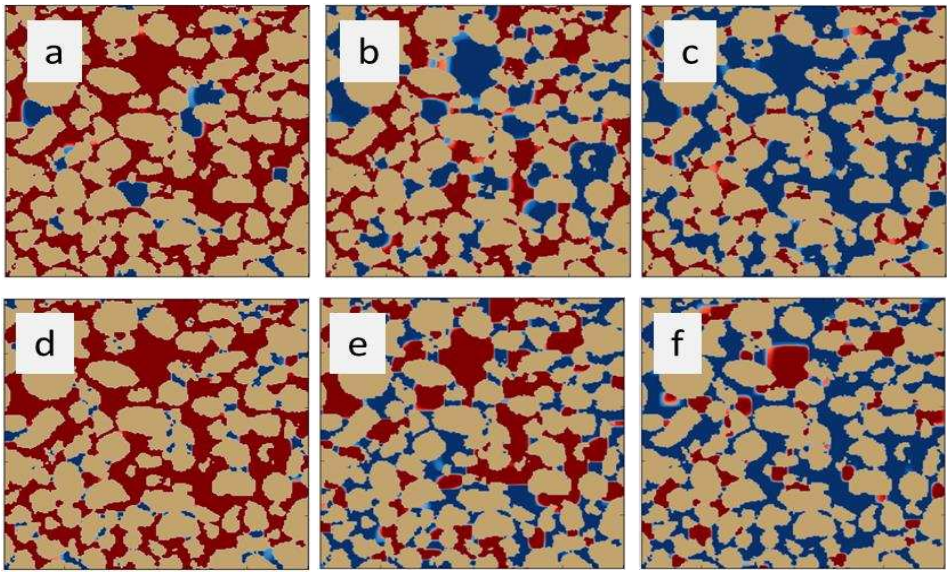

Figure 6.4: Simulation output for the equilibrium phase distribution of oil (red) and water (blue) confined to an Ottawa sand (brown) pore space. Panels a-c represent the pure water and heptane phases at a contact angle of 105°, panels d-e represent the 7.5% NaOH system with a contact angle of 70°. Panels a and d have saturation levels of 10 % water and 90% oil, panels b and e are 45% water and 55% oil, panels c and f are 75% water and 25% oil.

Several trends can be observed from Fig. 6.4. The first notable trend observed in the simulation results concerns the size distribution of the phases within the pore space. In the case of the plain water where the oil phase is more wettable, the water tends to form large pools in the larger areas of pore space in the system while the oil phase is

distributed through the smaller and tighter areas. In the system with 7.5% NaOH, the exact opposite trend is observed. Water is confined to the smaller pores and the oil phase is found in larger droplets in the larger areas of the pore space. Numerically this can be seen in Fig. 6.5 with observation of the surface area between the solid and fluid interfaces. The fluid that forms larger droplets in the larger pore space regions is in less contact with the solid phase. Fig. 6.5 shows that across the range of oil/water saturations, the solid-oil interfacial area is less than the solid-water interfacial area for the system doped with NaOH.

The major implication from this comes when considering recovering the phases from the pore space. While this simulation methodology is concerned with equilibrium phase distributions as opposed to flow properties that would simulate the removal of a phase, this methodology can still be used to ascertain insight into the relative ease in removing a phase from a pore space. Large droplets confined to larger pore ducts in a material require less energy to flow through the material. Smaller droplets confined to smaller areas and also possibly adsorbed to the solid phase will require significantly more energy to flow through the space. In a practical example, take a system 100% saturated with oil. Attempt to flush the pore space with water in effort to remove the oil. In a case where the water is more wettable than the oil on the solid phase, the oil phase will desorb from the solid and form large droplets which can flow readily through the larger channels of the pore network.

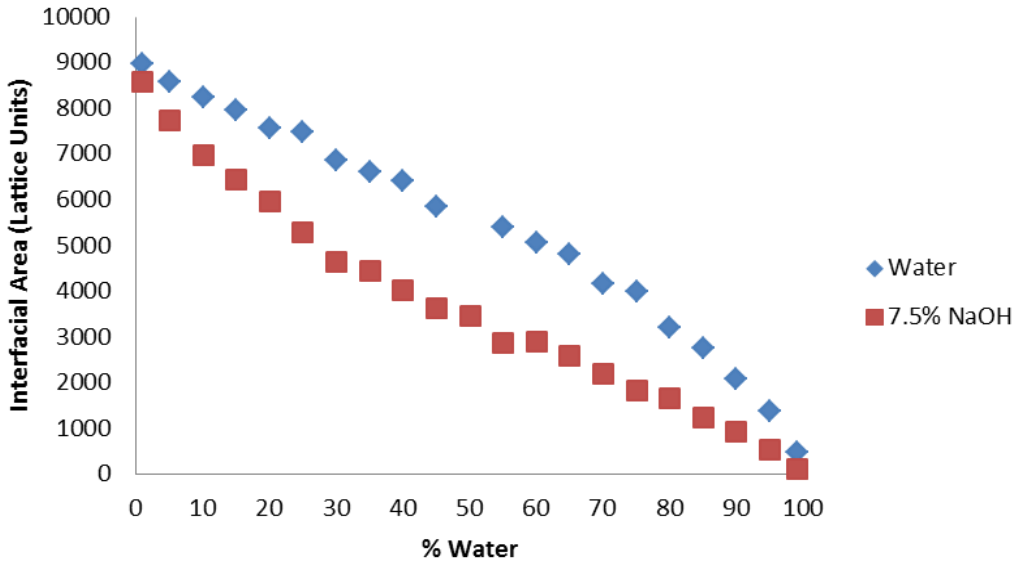

Figure 6.5: Plot of the interfacial area between oil and solid as a function of water saturation. The system with the 7.5% NaOH solution shows a smaller oil-solid interfacial area.

6.3. Conclusions

The Monte Carlo methodology has been modified for simulation of components beyond water and air. In this case two systems were examined were a wetting fluid and a non-wetting fluid corresponding to hydrate formation at geological timescales and two wetting fluids corresponding to water and oil competitively wetting within a pore space. The methodology can predict where, given long enough timescales, hydrate deposits are more likely to be found in sediments. With further development the methodology could be applied to the design of industrial systems that routinely encounter hydrate formation such as oil pipelines and drilling at the sea floor. In the case of two competitive wetting fluids, the methodology could be applied to the design of fracking fluids and technologies used to extract oil from unconventional reservoirs.

6.3. References Cited

[1] R. Knight, A. Chapman, and M. Knoll, “Numerical modeling of microscopic fluid distribution in porous media,” September 1989, pp. 994–1001, 1990.

[2] R. E. Jordan and J. A. Stark, “Capillary Tension in Rotting Ice Layers Cold Regions Research,” September, 2001.

[3] Z. M. Aman, S. E. Joshi, E. D. Sloan, A. K. Sum, and C. a Koh, “Micromechanical cohesion force measurements to determine cyclopentane hydrate interfacial properties.,” *J. Colloid Interface Sci.*, vol. 376, no. 1, pp. 283–8, Jun. 2012.

[4] K. L. Gering, “Simulations of methane hydrate phenomena over geologic timescales. Part 1: Effect of sediment compaction rates on methane hydrate and free gas accumulations,” *Earth Planet. Sci. Lett.*, vol. 206, no. 1–2, pp. 65–81, 2003.

[5] B. P. Binks and J. H. Clint, “Solid Wettability from Surface Energy Components: Relevance to Pickering Emulsions,” *Langmuir*, vol. 18, no. 4, pp. 1270–1273, Feb. 2002.

[6] M. T. Ghannam, “Spreading behavior of crude oil over limestone substrate,” *J. Colloid Interface Sci.*, vol. 262, no. 2, pp. 435–441, 2003.

CHAPTER 7

Conclusions and Future Work

The overall purpose of this work was to create a robust Monte Carlo simulation methodology to model phase distribution in porous materials with a geometrically complex pore space. Now we present a summary of the important results and a discussion of the future directions of this research.

7.1. Conclusions

Using Monte Carlo simulation to determine equilibrium distribution of phases within a pore space has the potential to simplify the calculation of important properties of partially wet porous materials. These calculations include the determination of constitutive properties such as equilibrium phase distribution, soil-water retention, and hysteretic isothermal adsorption curves. The major advantage to using this methodology as opposed to other simulation techniques is that this methodology prioritizes a close of a relationship as possible to experimental and natural systems. Input for this method consists of two major variables. The first being the pore space geometry. Since lattice gas models are algorithmically insensitive to complex geometries, simulation on any pore space system is possible. In many of the cases presented in the previous chapters, pore space geometry was discretized onto a lattice taken directly from experimental images (i.e microXCT of Ottawa sand). This allows for simulation to be performed without a compromise to the geometry of the pore space. From large complex interfaces to the small crevices between grains in a soil, all areas can be considered within the simulation domain. The second most important variable concerns

the interfacial energetics of the interfaces between the various phases in the simulation. Here to we determine these energetics directly from simulation. The simulation makes use of an interfacial coupling parameter that is directly related to experimental interfacial energies and can be determined in two differing ways. First, the literature or experimental values of the interfacial free energy (surface tension) can be used directly as the coupling parameters or modified according the equation $\gamma \approx 2J$ as discussed in the methodology sections of the preceding chapters. Since the actual equilibrium geometry is more closely related to the ratio of interfacial free energy between the various interacting phases, it is also possible to use contact angle measurements along with Young's equation to set the values of the coupling parameters. Throughout the studies contained herein, this approach was used. For systems involving water, air, and soil, the coupling parameters were set to using either simplified coupling parameters to achieve a perfect wetting (contact angle equal to 0) condition or with the literature/experimental values for the surface tension of water, air, and quartz. This approach was also utilized for studies of water, hydrates, and solid with literature surface tension values for the constituent phases. For the case of water, oil, and solid, both literature values for surface tension and contact angle were used to determine the interfacial coupling parameters. With the two major variable components being so closely related to experimental conditions, this approach allows for a simulation methodology that mirrors natural systems as closely as possible.

To begin validating our approach, we first considered applying the methodology in a constant liquid volume approach to geometries of increasing complexity. The details of this are found in chapter 4. We began by performing calculations on a system of two

identical spheres in contact to examine the water meniscus formed at equilibrium. Having verified that this water meniscus between the two spheres had the adsorbed liquid geometry we expected we next moved on to a system of randomly distributed spheres. Here the pore space geometry was set from an experimental study examining the water meniscus formed between randomly distributed glass beads. The results of the simulation on a similar system found that for systems with nearly identical volumetric water content, the equilibrium distribution of the water around the glass spheres showed excellent correlation between the simulation and experimental images. Having this excellent correlation, we then moved on to the most complex system we had experimental data available for: Ottawa sand. The results of this simulation showed a nearly identical equilibrium water distribution between experimental images and simulation. The simulation managed to capture many of the similar features of the equilibrium distribution including capillary bridges between grains and the location of trapped air bubbles within the pore space. In addition to the equilibrium capillary distribution, we were also able to calculate two major constitutive properties of partially wet soils. This includes both the soil-water retention curve and capillary specific surface area curve. Both curves also showed excellent agreement with experiment. Thus we considered our methodology validated for the determination of capillarity in porous media.

After our success with canonical constant volume simulation the natural extension of the project was to modify the simulation for grand canonical (constant humidity) simulation conditions. The details of this are discussed in chapter 5. A chemical potential gradient was used to achieve the desired humidity. In this study we

considered two pore space geometry, both of which were also used in the canonical study. These included the system of randomly distributed glass spheres and Ottawa sand. The first step was to use the methodology to calculate the isothermal adsorption curves under both drying and wetting conditions. This was done successfully and hysteresis between the drying and wetting paths was observed. More interesting was that the shape of these isotherms differed between the two geometries. Given that both simulation domains were identical in size (250x250 lattice units), this demonstrates that the simulation methodology is sensitive to the actual geometry of the pore space. This is important because isothermal adsorption with hysteresis is frequently used to determine the size, shape, and pore space distribution of materials. For the Ottawa sand system the soil-water retention was calculated and also showed very good correlation with experimental studies. The grand canonical study concluded with a discussion of hysteresis, metastability, and how these phenomena manifest within a lattice gas simulation. From these results we concluded that the grand canonical simulation methodology was successful in its application to wetting and drying hysteresis as seen in porous materials.

Since the system of water, air, and solid had now been fully explored in various pore space geometries and under both constant volume (canonical) and constant humidity (grand canonical) conditions, the next logical research direction was to perform simulation on systems of different substances. This is the focus of chapter 6. Two systems of different substances were chosen in support of energy research.

The first system was designed to approximate gas hydrate formation and agglomeration within a pore space at geological time scales. This implicitly amounts to a

system with a wetting fluid and a non-wetting fluid. For simplicity, interfacial free energy values were chosen to represent quartz, water, and ice. This system was studied using the standard Monte Carlo approach within multiple pore spaces. Starting with a simple system of two differently shaped square pores, the major result was that the hydrate always began to agglomerate and was confined in the largest pore. As more hydrate was added to the system, the agglomeration would continue to grow until it began to take on the geometry of the pore space. At a certain point, depending on pore size and system energetics, an additional agglomeration would form in the next largest pore space instead of continue to deform the original hydrate agglomeration. Based on this result we were able to use the pore space size distribution to predict where hydrate is likely to form in a complex pore space.

The second multiple component system considered was that of two comparative wetting fluids. In this case the system was used to approximate water and oil confined to a pore space. Interfacial free energy values used were for quartz, water, and heptane. Simulations were performed on two versions of this system, one with a contact angle of 105° and one with a contact angle of 70°. The major result here showed that the different contact angles would bias the equilibrium distribution of the fluids. In the case of the 105° contact angle, the oil phase would tend to be more confined to the smaller areas of the pore space while the water phase would be found in larger pools in the more expansive pores in the system. When the contact angle was reduced to 70°, this trend reversed. If the intended application is oil recovery form porous materials, this result shows that in a system of oil and water, a reduced contact angle can reduce the

energy required to recover the oil since it takes less energy to desorb material from a large expansive pore space than from a small narrow one.

7.2. Future Work

The diverse nature of this simulation methodology leads to many avenues for future study. These include simulation on three-dimensional pore spaces and modifying the methodology for microscale pore spaces and including forces beyond simple nearest neighbor interactions

7.2.1. Simulation in Three Dimensions.

With relatively little modification the simulation can easily be adapted to do calculations in three dimensions. The main qualification for three dimensional Monte Carlo to be an effective tool is in the availability of input data. In two dimensions input is only a digital image of the pore space which is converted into the coarse grained simulation domain. Imaging data would have to exist in a way that can be easily read into the simulation methodology.

Some preliminary work on this has approach already begun. Three dimensional tomographic imaging data exists for Ottawa sand. A sample domain of the Ottawa data was taken and sliced into a cube of dimensions 50x50x50. Figure 6.1 shows initial simulation results for this Ottawa sand sample at 50% liquid saturation. As this is a proof of concept simulation, the domain was only equilibrated for 50 Monte Carlo steps.

The major drawback to this approach is in computational time. As a Monte Carlo step is defined as the total number of locations within the lattice, as dimensionality is increased, the size of a Monte Carlo step grows exponentially. For the standard

simulations seen throughout the research herein, the simulation domain is 250x250 lattice units resulting in one Monte Carlo step being 62,500 attempted transitions. In two dimensions a simulation of 8000 Monte Carlo steps can be accomplished in a few hours. To maintain the same resolution but with a three dimensional pore space (250x250x250) one Monte Carlo step increases to 15,625,000 attempted transitions.

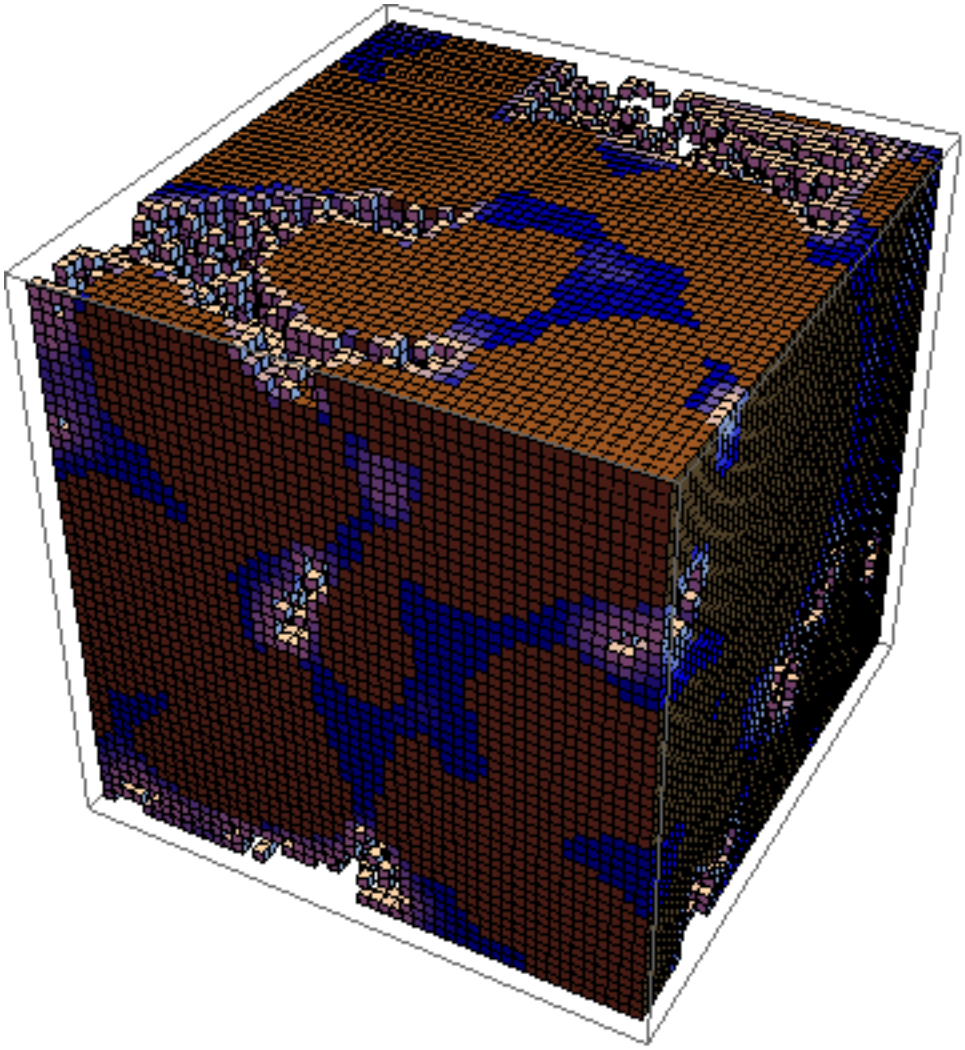

Figure 7.1: Rendering of a sample Monte Carlo simulation in three dimensions on Ottawa sand. Simulation domain is 50x50x50, brown indicates solid, blue water, and white is air. Simulation was equilibrated for 50 Monte Carlo steps. This is a time average over the entire simulation.

7.2.2. Simulation at the Microscale

Perhaps of more interest than three dimensional simulation, or in conjunction with three dimension simulation, is to use the methodology to investigate smaller pore sizes. The most studied system, Ottawa sand, has a lattice site dimensionality of approximately 15μm x 15μm. At this scale using interfacial the interfacial free energy (surface tension) works because the mobile phases in the pore spaces can be treated as bulk fluids. Under this assumption the interfacial free energy is the dominate contribution to the systems overall energy. While the simulation methodology is inherently size invariant (a lattice unit has no dimensionality during simulation), when the size of the pore space decreases, eventually the assumption about the free energy breaks down. When the size becomes small enough that the phases can no longer be considered bulk fluids, additional contributions to the energy need to be considered. In particular molecular interactions and Van Der Waals forces will need to be included. Practically, modifying the simulation for these additional forces would consist of nothing more than modifying the simulation's Hamiltonian to include terms for them. The difficulties in this modification come from finding sufficient experimental data for these forces, and applying this data to the simulation.

APPENDIX A

Simulation Methodology

This section discusses the methods used to set up a Monte Carlo simuation. It includes examples of the input file for the pore space geometry and simulation code.

A.1. Monte Carlo Simulation Method

There are two main variables that must be set by the user prior to running a simulation. The first variable is the input geometry. Inputting the simulation geometry involves selecting a two dimensional image representing the pore space that the simulation will be performed on. First, the image file resolution must match that of the simulation. For example, if the simulation resolutions is 250x250 lattice units, the corresponding input picture must have a size of 250x250 pixels. Examples of input files used in this work are given in figure A1. For the simulation to input the image file, the name of the image file must be specified in the simulation code. This is located at approximately line number 119, with the code:

sim_geometry = file_to_array(‘filename.png)

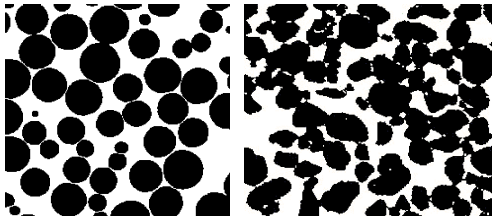

Figure A.1: Example of input images for Monte Carlo simulation. Left is randomly distributed spheres, right is Ottawa sand.

The other main input variables are the saturation levels. These are found at the bottom of the simulation code at lines 502 and 504. Here, one creates arrays for the saturations. In the example code given, this simulation is set up for hydrate and water. Simply set the

variables “hyds” and “wats” as arrays for each simulation. The code will automatically run new simulations for all of the saturation levels sent in these arrays. For example:

wats = [99,90,80]

hyds = [1,10,20]

will run 3 simulations at hydrate saturations of 1%, 10% and 20% with corresponding water saturations at 99%, 90%, and 80%. If these do not add up to 100, the remaining percent will be assigned as air.

A.2. Monte Carlo Simulation Subroutine Descriptions

- options(): This subroutine left empty for future use.
- sysvar(): This section defines the system variables: temperature, chemical potential, and coupling parameters for all interactions and is designed to be modified for each specific simulation type.
- file_to_array(): This section converts the input image into an array.
- gridsetup(): This section sets up all of the arrays needed for simulation. Here the user will specify the input file geometry.
- neighbors(): Samples nearest neighbor interactions.
- imagesaver(): and colorconverter(): These are responsible for image processing and output.
- sys_energy(): Calculates current system energy.
- int_area(): Calculates the interfacial area between the 2 specified phases.
- ising2d_4spin(): This is the main Monte Carlo algorithm for a 4-phase system.
- ising2d_kawas(): This is a Monte Carlo algorithm for a three phase system carried over from previous versions.

- hydrateMC(): This is the main routine. Here the user can specify all of the different types of outputs desired, as well as which subroutines are called. This subroutine writes all of the output files and calls the main Monte Carlo simulation.
- sequence(): The user specifies the saturation levels of the included phases here.

A.3. Simulation Code

```
"""
HydrateMC v. 1.0 - Ben Zeidman 2012, Colorado School of Mines
4-Phase Monte Carlo lattice simulation in random granular distributions.

Phase Assignments:
1 - Water
2 - Hydrate
3 - Air
4 - Solid

This simulation displays both water and hydrate image,
as well as two data output files.


"""

from numpy import *
from scipy import *
import random
import matplotlib
import pylab
import time
import math
import cProfile

def options():
    return ;

def sysvar():
    #Define global system variables:
```

```
#Iterations: number of times to loop main algorithm:
#(100 - Short; 250 - Default; 350 - Long)

iterations = 250

#Temperature and Chemical Potential:

T = 1.0
mu = 1.0

#Define fill levels:
#For grand canonical simulations: Drying fill = 100; Wetting fill = 0

#water_fill = 10
#hydrate_fill = 20

#Coupling parameters:

Jwa = 3.6 #water-air
Jws = 17.7 #water-sand
Jsa = 21.3 #solid-air

Jhw = 2.6 #hydrate-water
Jha = 1 #hydrate-air
Jhs = 17 #hydrate-solid

Jww = 0.0 #water-water
Jaa = 0.0 #air-air
Jss = 0.0 #solid-solid
Jhh = 0.0 #hydrate-hydrate

#Define energy arrays:

water_energies = array([None, Jww, Jhw, Jwa, Jws])
hydrate_energies = array([None, Jhw, Jhh, Jha, Jhs])
air_energies = array([None, Jwa, Jha, Jaa, Jsa])

energy = array([[0,0,0,0,0], water_energies, hydrate_energies, air_energies],float)

return iterations, T, mu, energy;
```

```
def file_to_array(image_name):
    #Loads .png file as array:

    img = matplotlib.image.imread(image_name)
    img_grid = zeros((98,96))

    for x in range(98):
        for y in range(96):

            if all(img[x,y]) != all([0,0,0,1]):
                img_grid[x,y] = 3
            else:
                img_grid[x,y] = 4

    return img_grid

def gridsetup(water_fill, hydrate_fill):
    #Setup simulation domains

    xwatarr = []
    ywatarr = []

    xairarr = []
    yairarr = []

    xhydarr = []
    yhydarr = []

    N = 98
    M = 96

    main_grid = zeros((N,M))
    water_grid = zeros((N,M))
    hydrate_grid = zeros((N,M))
    air_grid = zeros((N,M))

    water_dense = zeros((N,M), float)
    hydrate_dense = zeros((N,M), float)
```

```
#Setup grain geometries from geometry files,
#plan to read fname form input file

sim_geometry = file_to_array('input.png')
sim_geometry = array(sim_geometry)

for x in range(N):
    for y in range(M):

        hfill = float(hydrate_fill)/100
        wfill = float(water_fill)/100

        Rfill = random.random()

        if sim_geometry[x,y] == 4:
            main_grid[x,y] = 4

        elif Rfill < wfill:

            main_grid[x,y] = 1
            water_grid[x,y] = 1

            xwatarr.append(x)
            ywatarr.append(y)

        elif Rfill > wfill and Rfill < (wfill+hfill):

            main_grid[x,y] = 2
            hydrate_grid[x,y] = 1

            xhydarr.append(x)
            yhydarr.append(y)

        #else:

            #main_grid[x,y] = 3
            #air_grid[x,y] = 1

            #xairarr.append(x)
            #yairarr.append(y)
```

```
        else:

            main_grid[x,y] = 1
            water_grid[x,y] = 1

            xwatarr.append(x)
            ywatarr.append(y)

    return N, M, main_grid, water_grid, hydrate_grid, air_grid, water_dense,
hydrate_dense, xwatarr, ywatarr, xhydarr, yhydarr, xairarr, yairarr;

def neighbors(M, N, xloc, yloc, thegrid):
    #Returns neighboring grid values (nR nL nU nD):

    return (thegrid[(xloc+1)%N,yloc], thegrid[(xloc-1)%N,yloc],
        thegrid[xloc,(yloc-1)%M], thegrid[xloc,(yloc+1)%M])

def imagesaver(fname,thing,cmap,cbar):
    #Saves images:

    pylab.figure(figsize=(10,10))
    ax = pylab.subplot(111)
    pylab.cla()
    pylab.imshow(thing, cmap)
    if cbar:
        pylab.colorbar(None)
    print 'Saving frame:', fname
    pylab.savefig(fname)

def colorconverter(uglygrid,N,M):

    prettygrid = zeros((N,M))

    for x in range(N):
        for y in range(M):

            if uglygrid[x,y] == 1:

                prettygrid[x,y] = .1
```

```
            elif uglygrid[x,y] == 2:

                prettygrid[x,y] = .4

            elif uglygrid[x,y] == 3:

                prettygrid[x,y] = 1.0

            elif uglygrid[x,y] == 4:

                prettygrid[x,y] = .8

    prettygrid[0,0] = 0
    prettygrid[0,1] = 1

    return prettygrid

def sys_energy(M, N, main_grid, energy):
    #Calculates system energy
    gridenergy = 0

    for y in range(M):
        for x in range(N):

            nR, nL, nU, nD = neighbors(M, N, x ,y, main_grid)

            #spin = main_grid[x,y]

            if main_grid[x,y] == 1 or main_grid[x,y] == 2 or main_grid[x,y] == 3:

                gridenergy += (energy[main_grid[x,y], nR] + energy[main_grid[x,y], nD])

    return gridenergy

def int_area(M, N, main_grid, type1, type2):
    #Calculates interface area, specify between which phases as type1, type2, when
calling

    gridarea = 0
```

```
    for y in range(M):
        for x in range(N):

            nR, nL, nU, nD = neighbors(M, N, x ,y, main_grid)

            if main_grid[x,y] == type1:

                if nR == type2:
                    gridarea += 1
                if nL == type2:
                    gridarea += 1
                if nU == type2:
                    gridarea += 1
                if nD == type2:
                    gridarea += 1


    return gridarea

def ising2d_4spin(M, N, T, mu, main_grid, water_grid, hydrate_grid, air_grid, energy,
xwatarr, ywatarr, xhydarr, yhydarr, xairarr, yairarr):
    #Kawasaki algorithm (constant volume)

    num_waters = size(xwatarr)
    num_hydrates = size(xhydarr)
    num_airs = size(xairarr)

    mc_steps = N*M

    for trans in range(2000000):

        #Choose one of three possible spin exchanges:

        #choice = random.randrange(3)
        choice = 1

        if choice == 0:
            #Water-Air
```

```
            index1 = random.randrange(num_waters)
            index2 = random.randrange(num_airs)

            arrayx1 = xwatarr
            arrayy1 = ywatarr

            arrayx2 = xairarr
            arrayy2 = yairarr

            grid1 = water_grid
            grid2 = air_grid

            main_grid, water_grid, air_grid, xwatarr, ywatarr, xairarr, yairarr =
ising2d_kawas(M, N, T, energy, index1, index2, arrayx1, arrayy1, arrayx2, arrayy2,
grid1, grid2, main_grid)

        elif choice == 1:
            #Water-Hydrate

            index1 = random.randrange(num_waters)
            index2 = random.randrange(num_hydrates)

            arrayx1 = xwatarr
            arrayy1 = ywatarr

            arrayx2 = xhydarr
            arrayy2 = yhydarr

            grid1 = water_grid
            grid2 = hydrate_grid

            main_grid, water_grid, hydrate_grid, xwatarr, ywatarr, xhydarr, yhydarr =
ising2d_kawas(M, N, T, energy, index1, index2, arrayx1, arrayy1, arrayx2, arrayy2,
grid1, grid2, main_grid)

        else:
            #Hydrate-Air

            index1 = random.randrange(num_hydrates)
            index2 = random.randrange(num_airs)
```

```
        arrayx1 = xhydarr
        arrayy1 = yhydarr

        arrayx2 = xairarr
        arrayy2 = yairarr

        grid1 = hydrate_grid
        grid2 = air_grid

        main_grid, hydrate_grid, air_grid, xhydarr, yhydarr, xairarr, yairarr =
ising2d_kawas(M, N, T, energy, index1, index2, arrayx1, arrayy1, arrayx2, arrayy2,
grid1, grid2, main_grid)
    return main_grid, water_grid, hydrate_grid, air_grid, xwatarr, ywatarr, xhydarr,
yhydarr, xairarr, yairarr


def ising2d_kawas(M, N, T, energy, index1, index2, arrayx1, arrayy1, arrayx2, arrayy2,
grid1, grid2, main_grid):
    #Constant Volume MC

    x1 = arrayx1[index1]
    y1 = arrayy1[index1]

    x2 = arrayx2[index2]
    y2 = arrayy2[index2]

    spin1 = main_grid[x1,y1]
    spin2 = main_grid[x2,y2]

    #Get the neighbors:

    nR1, nL1, nU1, nD1 = neighbors(M, N, x1 ,y1, main_grid)
    nR2, nL2, nU2, nD2 = neighbors(M, N, x2 ,y2, main_grid)

    #Calculate energies:

    E1_spin1 = energy[spin1, nR1] + energy[spin1, nL1] + energy[spin1, nU1] +
energy[spin1, nD1]
```

```
    E2_spin1 = energy[spin1, nR2] + energy[spin1, nL2] + energy[spin1, nU2] +
energy[spin1, nD2]

    E1_spin2 = energy[spin2, nR2] + energy[spin2, nL2] + energy[spin2, nU2] +
energy[spin2, nD2]
    E2_spin2 = energy[spin2, nR1] + energy[spin2, nL1] + energy[spin2, nU1] +
energy[spin2, nD1]

    dE = (E2_spin1 + E2_spin2) - (E1_spin1 + E1_spin2)

    #Do the Monte Carlo:

    if random.random() < e**((-dE)/T):

        main_grid[x1,y1] = spin2
        main_grid[x2,y2] = spin1

        arrayx1[index1] = x2
        arrayy1[index1] = y2

        arrayx2[index2] = x1
        arrayy2[index2] = y1

        grid1[x1,y1] = 0
        grid1[x2,y2] = 1

        grid2[x1,y1] = 1
        grid2[x2,y2] = 0

    return main_grid, grid1, grid2, arrayx1, arrayy1, arrayx2, arrayy2;

def hydrateMC(water_fill, hydrate_fill):
    #Main Routine

    transitions = 0


    #Get system parameters, initialize, setup grids, etc...
    iterations, T, mu, energy = sysvar()
```

```
    N, M, main_grid, water_grid, hydrate_grid, air_grid, water_dense, hydrate_dense,
xwatarr, ywatarr, xhydarr, yhydarr, xairarr, yairarr = gridsetup(water_fill, hydrate_fill)

    maingridcolors = colorconverter(main_grid, N, M)
    fname = "initial.png"
    imagesaver(fname, maingridcolors, cmap = pylab.cm.gist_earth, cbar = True)

    #Open the energy and interface area file:
    f0 = open("energy_interface_w_%03d_h_%03d.txt" % (water_fill, hydrate_fill), "w")
    f0.write('trans,energy,hyd-wat,wat-air,hyd-air,wat-sol,hyd-sol\n')

    while transitions < iterations:

        main_grid, water_grid, hydrate_grid, air_grid, xwatarr, ywatarr, xhydarr, yhydarr,
xairarr, yairarr = ising2d_4spin(M, N, T, mu, main_grid, water_grid, hydrate_grid,
air_grid, energy, xwatarr, ywatarr, xhydarr, yhydarr, xairarr, yairarr)
        transitions +=1

        #Calculate energy and interface areas then write them to the file:
        sysenergy = sys_energy(M, N, main_grid, energy)
        hydwatint = int_area(M, N, main_grid, type1 = 2, type2 = 1)
        watairint = int_area(M, N, main_grid, type1 = 1, type2 = 3)
        hydairint = int_area(M, N, main_grid, type1 = 2, type2 = 3)
        watsolint = int_area(M, N, main_grid, type1 = 1, type2 = 4)
        hydsolint = int_area(M, N, main_grid, type1 = 2, type2 = 4)
        f0.write('%d, ' % transitions)
        f0.write('%d, ' % sysenergy)
        f0.write('%d, ' % hydwatint)
        f0.write('%d, ' % watairint)
        f0.write('%d, ' % hydairint)
        f0.write('%d, ' % watsolint)
        f0.write('%d, ' % hydsolint)
        f0.write('\n')

        #Update densities:
        if transitions > iterations - ((iterations / 5) * 4):
            hydrate_dense += hydrate_grid
            water_dense += water_grid

        #Image saves for diagnostics:
```

```
    #fname1 = "_main%03d.png" % transitions
    #fname2 = "_waters%03d.png" % transitions
    #fname3 = "_hydrates%03d.png" % transitions

    #imagesaver(fname2, water_grid, cmap = None, cbar = False)
    #imagesaver(fname3, hydrate_grid, cmap = None, cbar = False)

    #maingridcolors = colorconverter(main_grid, N, M)
    #imagesaver(fname1, maingridcolors, cmap = pylab.cm.gist_earth, cbar = False)

    print "Iteration", transitions, "out of", iterations, "Hydrate level: ",hydrate_fill

f0.close()

#Image final frame:
#maingridcolors = colorconverter(main_grid, N, M)
#fname = "final.png"
#imagesaver(fname, maingridcolors, cmap = pylab.cm.gist_earth, cbar = False)



#Write the output files:

hydrate_dense = hydrate_dense / (iterations - ((iterations / 5) * 4))
water_dense = water_dense / (iterations - ((iterations / 5) * 4))

f1 = open("hydrate_density_w_%03d_h_%03d.txt" % (water_fill, hydrate_fill), "w")
f2 = open("water_density_w_%03d_h_%03d.txt" % (water_fill, hydrate_fill), "w")

for x in range(N):
    for y in range(M):

        f1.write('%0.3f     ' % hydrate_dense[x,y])
        f2.write('%0.3f     ' % water_dense[x,y])

    f1.write("\n")
    f2.write("\n")

f1.close()
f2.close()
```

```
#Display the final image:

#display hydrates and water seperately as diagnostic
#fname1 = "hydratefinal.png"
#fname2 = "waterfinal.png"
#imagesaver(fname1, hydrate_dense, cmap = pylab.cm.Greens, cbar = False)
#imagesaver(fname2, water_dense, cmap = pylab.cm.Blues, cbar = False)

dirt_grid = zeros((N,M))

for x in range(N):
    for y in range(M):

        if hydrate_dense[x,y] <= water_dense[x,y]:
            hydrate_dense[x,y] = None

        if main_grid[x,y] == 4:
            dirt_grid[x,y] = .8

        else:
            dirt_grid[x,y] = None

#Set normalization for colormap to work
dirt_grid[0,0] = 0
dirt_grid[0,1] = 1
hydrate_dense[0,0] = 0
hydrate_dense[0,1] = 1
water_dense[0,0] = 0
water_dense[0,0] = 1




imname = "final_w_%03d_h_%03d.png" % (water_fill, hydrate_fill)
pylab.cla()
pylab.imshow(water_dense, cmap = pylab.cm.Blues)
pylab.imshow(hydrate_dense, cmap = pylab.cm.OrRd)
pylab.imshow(dirt_grid, cmap = pylab.cm.gist_earth)
print 'Saving frame:', imname
```

```
    pylab.savefig(imname)

#hydrateMC()

def sequence():

    wats = [99,95,90,85,80,75,70,65,60,55,50]

    hyds = [1 ,5 ,10,15,20,25,30,35,40,45,50]

    for runs in range(len(wats)):

        hydrateMC(wats[runs],hyds[runs])


sequence()
```

APPENDIX B

Experimental Methods

The experimental method to determine the soil-water retention curve (SWRC) seen in Chapter 5 is based off of methodology developed by Lu et al. (2012) [1]. The working principle of the method is that as soil is exposed to an increase in suction, water outflow is observed, and a sudden decrease in suction water is imbibed back into the soil sample. The mass of the water outflow of the system coupled with inverse modeling allows for the calculation of the SWRC.

The methodology is broken into eight distinct parts. First the sample is prepared and placed into the flowcell (Fig. B.1b) and the porosity is calculated. Second, the system is fully saturated with water and all air bubbles are removed. Third, the data logging system is initiated and an interval is set to record mass and applied pressure (every 5 minutes for the data in Chapter 5). Fourth, a small suction increment is applied to the system while water outflow is observed and recorded. Fifth, a large suction increment is applied and the water outflow versus time is observed and recorded. Step six is used to quantify the airflow through the ceramic disk. These are quantified by flushing them to the air bubble trap (Fig. B1d). Step seven involves the application of wetting conditions to the sample. The applied pressure is decreased and the mass of water inflow is recorded. Step eight is the calculation of the SWRC from the experimental data. The raw experimental output data for the SWRC calculations in Chapter 5 is shown in figure B.2.

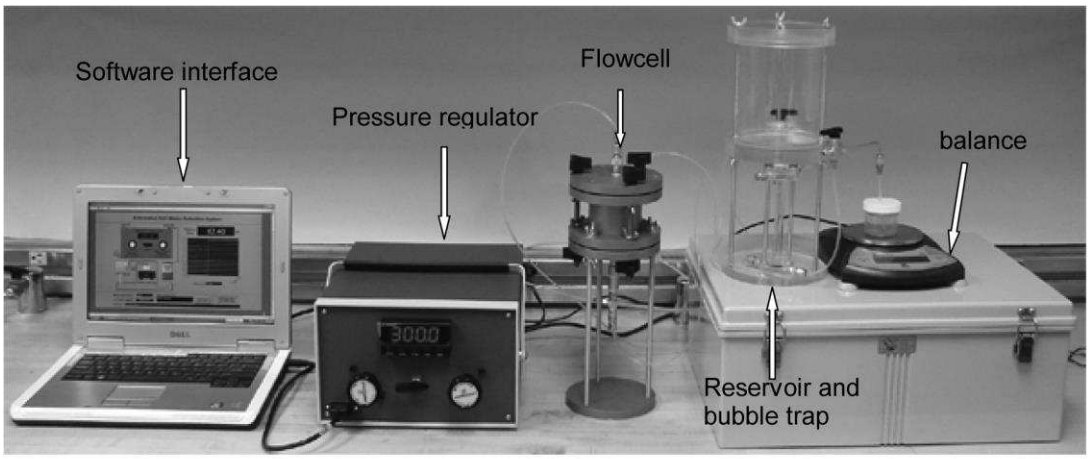

(a)

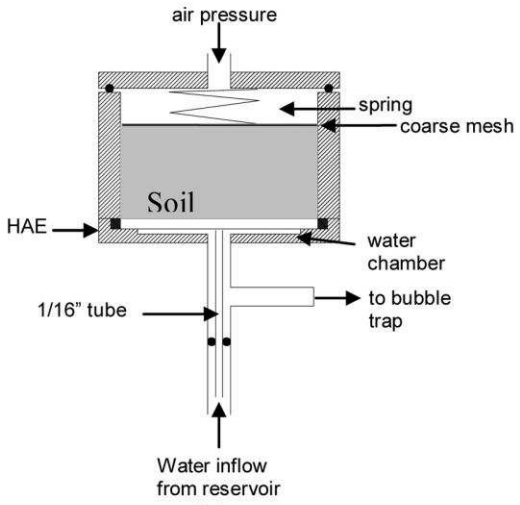

(b)

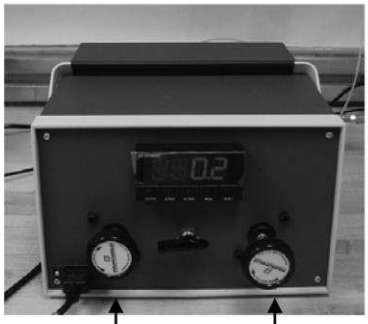

(c)

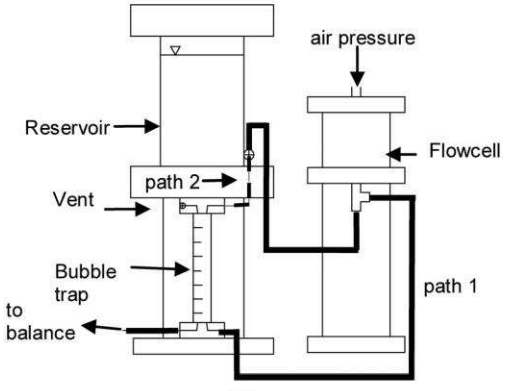

(d)

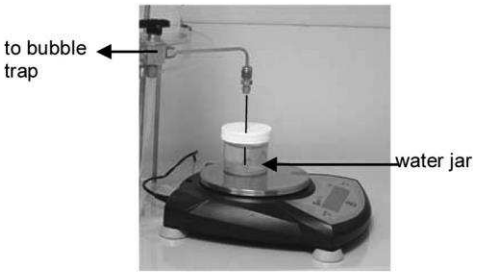

(e)

Figure B.1: Apparatus used in the experimental method. (a) is a photograph of the entire experimental setup, (b) is a diagram of the flowcell, (c) is the pressure regulator, (d) is the air flushing system, and (e) is the balance used to measure the mass of water outflow form the soil sample.

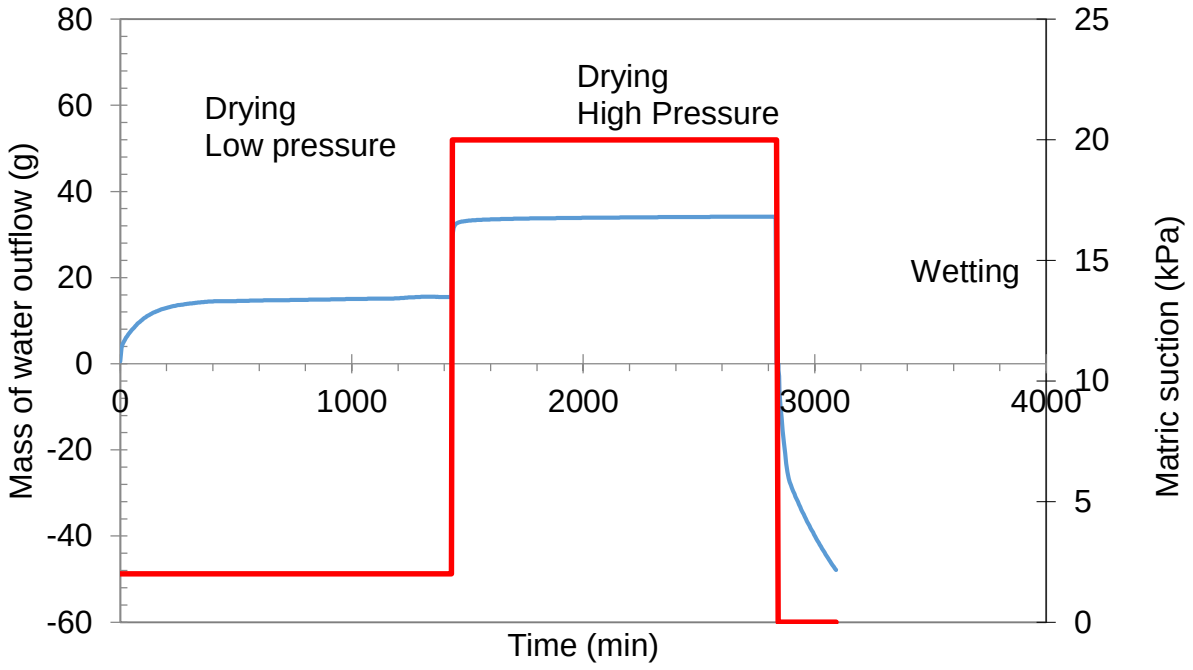

Figure B.2: Raw data output for the SWRC calculation.

Works Cited:

[1] A. Wayllace and N. Lu, “A Transient Water Release and Imbibitions Method for Rapidly Measuring Wetting and Drying Soils Water Retention and Hydraulic Conductivity Functions” *Geotechnical Testing Journal,* vol. 35, no. 1, GTJ103596, (2012).

APPENDIX C

Copyright and Permissions

Chapter 3:

Permission obtained from World Scientific, Tu Ning, rights@wspc.com

Reprinted with Permission of World Scientific: B.D. Zeidman, N. Lu, and D. Wu, "Coarse-Grained Monte Carlo Simulation of the Distribution and Capillarity of Multiple Fluids in Porous Media" in Pore Scale Phenomena: Frontiers in Energy and Environment, edited by J. Poate, T. Illangasekare, H. Kazemi, and R. Kee (World Scientific, Singapore, 2015), pp. 263-278

Chapter 4:

Clinton S. Willson on 3-27-2016:

“You have my permission to use the manuscript (A Monte Carlo Paradigm for Capillarity in Porous Media, published in GRL in 2010) that I was a co-author on for reuse in your dissertation. Please don't hesitate to let me know if you need anything else.”

Mark T. Lusk on 3-28-2016:

“You certainly have permission from me to use the information in any way or form that you deem appropriate, form our join paper, “A Monte Carlo Paradigm for Capillarity in Porous Media”, in your dissertation”

Geophysical Research Letters:

JOHN WILEY AND SONS LICENSE
TERMS AND CONDITIONS
Mar 28, 2016

This Agreement between Ben Zeidman ("You") and John Wiley and Sons ("John Wiley and Sons") consists of your license details and the terms and conditions provided by John Wiley and Sons and Copyright Clearance Center.

License Number	3837340627378
License date	Mar 27, 2016

Licensed Content Publisher	John Wiley and Sons
Licensed Content Publication	Geophysical Research Letters
Licensed Content Title	A Monte Carlo paradigm for capillarity in porous media
Licensed Content Author	Ning Lu,Benjamin D. Zeidman,Mark T. Lusk,Clinton S. Willson,David T. Wu
Licensed Content Date	Dec 7, 2010
Pages	1
Type of use	Dissertation/Thesis
Requestor type	Author of this Wiley article
Format	Electronic
Portion	Full article
Will you be translating?	No
Title of your thesis / dissertation	Monte Carlo Simulations of Phase Distribution in Porous Materials
Expected completion date	May 2016
Expected size (number of pages)	110
Requestor Location	Ben Zeidman 1500 Illinois St GOLDEN, CO 80401 United States Attn: Ben Zeidman
Billing Type	Invoice
Billing Address	Ben Zeidman 1500 Illinois St GOLDEN, CO 80401 United States Attn: Ben Zeidman